

Coupling free-surface geometry and localized ion dose for continuum models of radiation-induced nanopatterning

Tyler P. Evans^{*1} and Scott A. Norris²

¹Department of Mathematics, University of Utah, Salt Lake City, UT 84112, United States of America

²Department of Mathematics, Southern Methodist University, Dallas, TX 75275, United States of America

October 3, 2025

Abstract

A first-principles understanding of the self-organization of highly regular, nanometer-scale structures atop irradiated semiconductor surfaces has been sought for decades. While numerous models exist which explain certain aspects of this phenomenon, a unified, physical model capable of explaining all details of pattern formation has remained elusive. However, it is increasingly apparent that such a model will require understanding the dual influence of the collision cascade initiated by ion implantation: first, as a source of material transport by sputtering and atomic displacements occurring over short time scales, and, second, as a source of defects permitting viscous flow within the thin, amorphous layer that results from sustained irradiation over longer time scales. To better understand the latter, we develop several asymptotic approximations for coupling the localized ion dose with an evolving free interface. We then show how theoretical predictions of quantities commonly used for comparison with experimental observations — such as ripple wavelengths, critical irradiation angle for patterning onset, and surface roughening — exhibit surprising sensitivity to the details of this coupling.

Contents

1	Introduction	2
2	Asymptotic approximations	3
2.1	Free surface of single wavenumber and small amplitude	4
2.2	Free surface of small curvature	9
3	Application to continuum model	11
3.1	Governing equations	11
3.2	Linear growth rates	12
3.3	Weakly nonlinear evolution	13
4	Results	15

^{*}Corresponding author: evans.tyler@utah.edu, <https://orcid.org/0000-0001-7812-2479>

5 Discussion	18
A Further calculation details: linear regime	19
B Further calculation details: weakly-nonlinear PDE	20

1 Introduction

When subjected to broad-beam ion irradiation, semiconductor surfaces may spontaneously self-organize into highly regular patterns with characteristic lengths on the order of nanometers; see, for example, [49, 6]. The possibility of exploiting this phenomenon to mass-produce nano-engineered surfaces remains appealing and has been discussed [10, 31, 30, 46, 56, 19]. At the same time, the lack of a fully explanatory theory of this phenomenon continues to pose a now decades-old puzzle [10, 46, 56, 19].

Initial attempts at a theoretical explanation centered around surface erosion via the Bradley-Harper instability [66, 67, 3, 4], which were soon followed by considering the redistribution of atoms not sputtered away [7, 5, 52, 54, 57, 55]. Eventually, it was realized that, due to ion-induced structural changes, the first few nanometers of the irradiated semiconductor surface behave as a thin fluid film of extremely high viscosity [65, 77]. This provoked a great deal of interest in connecting the classical theory of hydrodynamic instability [21, 12], and more recent pattern formation theory [16, 15], to the problem of ion-induced self-organization of semiconductor surfaces. Numerous such hydrodynamic-type models emerged where the amorphous layer and the creation and relaxation of ion-induced stresses were central to pattern formation phenomena [18, 9, 8, 51, 44, 69, 22, 24, 25], in contrast with models focused on erosion and redistribution. Some hydrodynamic models, even if phenomenological, appeared to give good agreement with θ_c and $\lambda(\theta)$ for at least a subset of possible experimental systems, such as [51, 44]. Increasingly, it appears that a combination of erosion, redistribution, and viscous flow effects govern pattern formation, particularly at low energies [53, 39, 47, 48].

To assess agreement between theory and experiment, several points of comparison can be considered. The bifurcation angle or critical angle, θ_c , is the minimal angle away from normal incidence at which pattern formation begins [44, 56]. At irradiation angles below this (i.e., closer to normal-incidence), surfaces remain flat, or smoothen. For a given ion, target, and energy combination, θ_c varies, and this non-universality provides a benchmark test for proposed theoretical models [44, 56]. A second benchmark test is given by the irradiation angle-dependent ripple wavelength formed at low fluences, denoted $\lambda(\theta)$ [42, 18, 9, 43, 63, 44]. Theoretical predictions of both θ_c and $\lambda(\theta)$ are commonly extracted from models using linear stability analysis [18, 9, 8, 51, 44, 22, 24, 25].

Common to all models is the understanding that ion implantation — or the resulting collision cascade — is ultimately responsible for all of the physics relating to pattern formation: erosion, redistribution, stresses, and fluidity [10, 38, 46, 56, 19]. As irradiation drives surface evolution, the localized fluence of radiation received by the amorphous layer through the deformed free surface varies with the surface geometry. This produces a complex, multilateral coupling between the influence of the collision cascade, the free interface, and the amorphous layer's fluid-like dynamics, regardless of the exact, underlying theoretical model. Contributing to the difficulty of developing a unifying model of ion-induced pattern formation, the collision cascade shape depends greatly on ion and target species, and energy [85, 86, 10, 38, 56], although only weakly on irradiation angle [32, 28].

Within the hydrodynamic class of models, numerous *ad hoc* modeling choices have been made about, e.g., material response to irradiation [18, 9, 8, 51, 44, 69, 22, 24, 25] and the geometry of the

amorphous-crystalline interface. This interface has been treated variously as flat [50, 45], a vertical translation of the free interface [51], or a diagonal (downbeam) translation of the free interface [44, 69]. Later, it was shown that the relationship between the free and amorphous-crystalline interfaces, on its own, exerts a strong influence on the bifurcation angle θ_c and the irradiation angle-dependent wavelength $\lambda(\theta)$ [44, 24]. Towards developing a realistic amorphous-crystalline boundary, [25] obtained a closed-form approximation of the amorphous-crystalline interface shape, valid in the long-wave limit, in terms of the collision cascade shape. Moreover, [25] showed the stabilizing effect of phase-change at the amorphous-crystalline boundary and sensitive dependence of this effect on the boundary's shape and location, offering a possible explanation for the strong suppression of ripples for Ar-irradiated Si at energies between around 1.5keV and 20keV [29]. We therefore posit that an eventual, unified model of self-organized pattern formation in irradiated semiconductors could depend rather sensitively on a realistic treatment of key aspects of the thin film, including the interfacial geometry, boundary conditions, and depth-dependent stress generation and relaxation.

In this paper, we develop asymptotic approximations relating the shape of the ion-induced collision cascade to localized ion dose in the amorphous layer through a deformed free interface. From this, we obtain depth-dependence profiles and closed-form relationships between free and amorphous-crystalline interfaces which are suitable for incorporation into both linear stability analyses and weakly nonlinear evolution equations obtained via, e.g., lubrication theory or gradient expansion [59, 14, 1, 45]. This includes generalizing our own work [25] beyond the long-wave limit to interfaces perturbed by sinusoids of *arbitrary* wavenumber. Importantly, these approximations are valid for *any* hydrodynamic model, under mild assumptions, and can be thought of as a continuum analogue of calculations for erosion rates conducted elsewhere [3, 4].

With these mathematical results in hand, we then consider some of their implications for a particular continuum model of ion-induced nanopatterning [25]: (i) how a depth-dependence coupled to the implanted ion distribution changes the strength of ion-induced swelling (IIS), recently-identified as a pattern-suppressing mechanism [69, 22, 24]; (ii) how a precise treatment of the amorphous-crystalline interface modifies the wavelength predictions of [51]; and (iii) how a precise treatment of deposition could influence surface evolution based on a nonlinear partial differential equation (PDE) which we newly derive from our continuum model using a lubrication theoretic approach [59, 14, 1]. We show that the geometry of the collision cascade, by influencing the depth-dependent production of ion-induced stresses and the amorphous-crystalline interface, can drastically change theoretical predictions for θ_c , $\lambda(\theta)$, surface roughening rates, and roughness at saturation. We anticipate that these long-overlooked details will be crucial in developing theoretical models suitable for comparison with experimental observations while minimizing *ad hoc* modeling choices and free, tuneable parameters [56].

2 Asymptotic approximations

Essentially all existing models of ion-induced pattern formation posit a key role for the *collision cascade*—the sequence of atomic recoils induced by a newly implanted ion [36, 83, 20, 38, 82]. The main difference between models concerned primarily with erosion and redistribution [3, 52, 54, 55, 4] and those concerned primarily with stress production and relaxation [65, 77, 11, 51, 33] is how the collision cascade is mechanistically linked to pattern formation.

Over many implantations through the same patch of surface, the statistically-averaged distribution of a deposited quantity (such as ions or energy) is well-approximated as a Gaussian ellipsoid [10, 32, 28]. Deposition can be lessened by *geometric flux dilution* [56]. Deposition of ions originating from patches of surface that are normal to incoming ions occurs at a greater rate than that

originating from patches locally parallel to incoming ions. Hence the influence of ion-implantation on surface evolution is modified by the geometry of the evolving surface. The integral

$$D_f(x, z, t) = \int_{-\infty}^{\infty} \frac{\cos(\theta) + h_X \sin(\theta)}{\sqrt{1 + h_X^2}} \Psi(x, z; X, h(X, t)) dX \quad (1)$$

provides the flux-diluted deposition of ions (“ion dose”) at each point (x, z) in the amorphous bulk given uniform irradiation across the surface $h(X, t)$. Ion implantation, recoils, and energy deposition all (at least approximately) follow the form of a Gaussian ellipsoid [66, 67, 3, 10, 4, 32, 28, 56],

$$\Psi(x, z; X, h(X, t)) = \frac{\Psi_0}{2\pi\alpha\beta} e^{\left(-\frac{[(x-X)\sin(\theta)-(z-h(X,t))\cos(\theta)-a]^2}{2\alpha^2} - \frac{[(x-X)\cos(\theta)+(z-h(X,t))\sin(\theta)]^2}{2\beta^2}\right)}, \quad (2)$$

where a, α, β, Ψ_0 are the mean downbeam implantation depth, downbeam standard deviation, cross-beam standard deviation, and total deposition per ion, respectively. The function above describes the probability of an ion aimed at the surface at location $(X, h(X, t))$ becoming deposited at position (x, z) . The same form has been used elsewhere in order to study surface erosion rates due to deposited energy, leading to the classical Bradley-Harper instability [3]. While thorough analyses of (1) exist for the erosive-distributive family of models [3, 17, 4], such an analysis is lacking for the hydrodynamic family of models. The main purpose of this work is to provide such an analysis, with special attention to useful limits, and their implications for theoretical predictions.

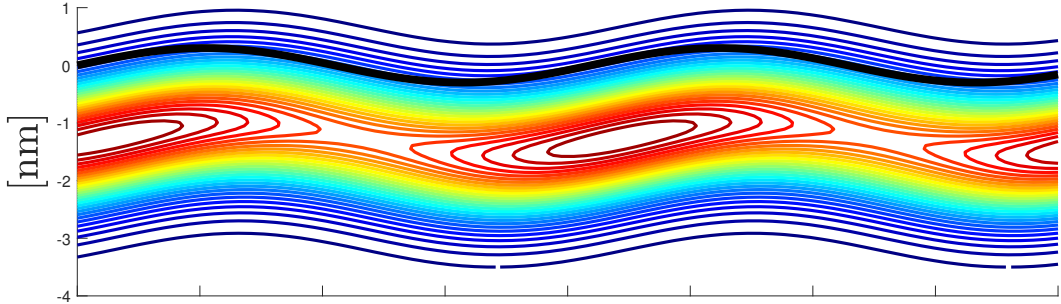


Figure 1: Example of level sets of localized dose (or fluence) of ions through a deformed free surface (black curve) at $\theta = 45^\circ$ off-normal incidence according to Equation 1. Red regions receive the highest local dose, and purple regions receive the lowest. We have supposed that the free interface is described by $h(X, t) = \frac{3}{10} \sin\left(\frac{3X}{10}\right)$. We choose parameters associated with 250eV Ar^+ irradiation of Si: $a = 1.8$ nm, $\alpha = 0.7$ nm, and $\beta = 0.8$ nm [85]. Where the intensity of ion implantation falls off, the amorphous-crystalline interface begins. The goal of the first part of this paper is to determine closed-form expressions for (i) the amorphous-crystalline interface and (ii) the local, depth-dependent dose as a function of the vertical (z) axis and wavenumber k .

2.1 Free surface of single wavenumber and small amplitude

Here, we obtain a general expression for the deposition functional expanded in sinusoidal perturbations of small amplitude and a single wavenumber. From this, we obtain the deposition profile in the irradiated bulk. Then, we consider level sets of the deposition field in order to obtain a theoretical description of the amorphous-crystalline boundary.

Expansion with geometric flux dilution. While (1) cannot be evaluated in closed-form for an arbitrary surface $h(X, t)$, it *can* be approximated in the limit of small, sinusoidal perturbations of a single wavenumber to an otherwise flat surface,

$$h(X, t) = \epsilon \tilde{h}_1 e^{\Sigma t + ikX}. \quad (3)$$

Expanding in ϵ and integrating, we obtain

$$D_f(x, z) = D_{f0}(z) + \epsilon \tilde{h}_1 \exp(\Sigma t + ikx) D_{f1}(z) + \mathcal{O}(\epsilon^2), \quad (4)$$

where

$$D_{f0}(z) = \frac{\Psi_0 \cos(\theta)}{\sqrt{2\pi(\alpha^2 c^2 + \beta^2 s^2)}} \exp\left(-\frac{(z + ac)^2}{2(\alpha^2 c^2 + \beta^2 s^2)}\right) \quad (5)$$

and

$$D_{f1}(z) = \frac{\Psi_0 \cos(\theta)}{2\sqrt{\pi A} \alpha^3 \beta^3} \exp\left(\frac{\tilde{B}^2(z)}{4A} - C(z)\right) \left[c_1(z) - c_2 \frac{\tilde{B}(z)}{2A} \right]. \quad (6)$$

In the above,

$$\begin{aligned} c_1(z) &= z(\alpha^2 \sin^2(\theta) + \beta^2 \cos^2(\theta)) + \cos(\theta) a \beta^2 + ik \alpha^2 \beta^2 \tan(\theta) \\ c_2 &= \cos(\theta) \sin(\theta) (\alpha^2 - \beta^2), \end{aligned}$$

and

$$\begin{aligned} A &= \frac{\beta^2 s^2 + \alpha^2 c^2}{2\alpha^2 \beta^2}; \quad B(z) = \frac{z s c (\alpha^2 - \beta^2) - a \beta^2 s}{\alpha^2 \beta^2}; \\ \tilde{B}(z) &= \frac{z s c (\alpha^2 - \beta^2) - a \beta^2 s}{\alpha^2 \beta^2} + ik; \quad C(z) = z^2 \frac{\beta^2 c^2 + \alpha^2 s^2}{2\alpha^2 \beta^2} + z \frac{a c}{\alpha^2} + \frac{a^2}{2\alpha^2}. \end{aligned}$$

where $c = \cos(\theta)$, $s = \sin(\theta)$, and k is the wavenumber of surface perturbation in nm⁻¹.

Expansion without geometric flux dilution. Now we revisit the calculation above where there is no flux dilution. We obtain

$$D(x, z) = D_0(z) + \epsilon \tilde{h}_1 \exp(\Sigma t + ikx) D_1(z) + \mathcal{O}(\epsilon^2), \quad (7)$$

where all dependence on x is carried by the leading exponential at $\mathcal{O}(\epsilon)$, and all dependence on z is described by

$$D_0(z) = \frac{\Psi_0}{\sqrt{2\pi(\alpha^2 c^2 + \beta^2 s^2)}} \exp\left(-\frac{(z + ac)^2}{2(\alpha^2 c^2 + \beta^2 s^2)}\right), \quad (8)$$

which is simply a Gaussian in the depth z , and

$$\begin{aligned} D_1(z) &= \frac{\Psi_0}{\alpha^2 \beta^2 \sqrt{2\pi(\alpha^2 c^2 + \beta^2 s^2)}} \exp\left(\frac{\tilde{B}(z)^2}{4A} - C(z)\right) \times \\ &\left[z(\alpha^2 s^2 + \beta^2 c^2) + ca \beta^2 - cs(\alpha^2 - \beta^2) \frac{(z s c (\alpha^2 - \beta^2) - a \beta^2 s + ik \alpha^2 \beta^2)}{(\alpha^2 c^2 + \beta^2 s^2)} \right]. \end{aligned} \quad (9)$$

Discussion. In [25], $x_0(\theta)$ and $h_0(\theta)$ are derived by the superposition of a sequence of Gaussian ellipsoids modeling deposited power or ions. The derivation of [25] is inherently long-wave: it assumes that the free surface varies over lengths much larger than the radius of the ellipsoid used to model deposition. For this reason, this result has been described as an “ellipse-dragging” approximation. This approximation has produced good agreement with $h_0(\theta)$ obtained via fits to GISAXS data [53]. It also agrees well with $h_0(\theta)$ determined via MD simulation [44] and TEM imaging [44].

However, [25] also showed that the amorphous-crystalline interface shape strongly influences θ_c and $\lambda(\theta)$. $h_0(\theta)$ also affects the inference of in-plane stresses from angle-dependent wafer curvature data [62, 24]. The apparent sensitivity of modeling efforts to the amorphous-crystalline interface invites caution. Accordingly, we observe that the linearized deposition field obtained above is applicable for perturbations to the free surface of arbitrary wavenumber k ; hence it may be used to obtain the amorphous-crystalline interface shape *directly* as a level set of deposition.

Formal calculation of amorphous-crystalline interface. Proceeding from the linearized deposition field (7), where a macroscopically flat free surface is slightly perturbed by a single sinusoid of fixed wavenumber, we seek level curves

$$z = g_0 + \epsilon \tilde{g}_1 \exp(\Sigma t + ikx), \quad (10)$$

such that

$$D(x, z) = D_0(z) + \epsilon \tilde{h}_1 \exp(\Sigma t + ikx) D_1(z) + \mathcal{O}(\epsilon^2) = D_c, \quad (11)$$

where D_c is some critical threshold beyond which amorphization proceeds. We will solve for g_0 and \tilde{g}_1 . For our purposes, we first establish D_c by computing the first and second central moments, M_1 and M_2 , of the linearized deposition field. By definition,

$$\begin{aligned} M_1 &= \int_{-\infty}^{\infty} z(D_0(z) + \epsilon \tilde{h}_1 \exp(\Sigma t + ikx) D_1(z)) dz, \\ M_2 &= \int_{-\infty}^{\infty} z^2(D_0(z) + \epsilon \tilde{h}_1 \exp(\Sigma t + ikx) D_1(z)) dz, \end{aligned} \quad (12)$$

and we adopt the notation

$$\begin{aligned} M_1 &= M_{10} + \epsilon \tilde{h}_1 \exp(\Sigma t + ikx) M_{11} \\ M_2 &= M_{20} + \epsilon \tilde{h}_1 \exp(\Sigma t + ikx) M_{21}. \end{aligned} \quad (13)$$

Then we define $D_c = D(x, z = \mu - 2\sigma)$, so that the amorphization threshold is assigned as two standard deviations σ away from the mean μ and into the irradiated substrate, where $\mu = M_1$ and $\sigma = \sqrt{M_2 - M_1^2}$. Expanding in ϵ , we compute

$$\begin{aligned} \mu &= \mu_0 + \epsilon \tilde{h}_1 \exp(\Sigma t + ikx) \mu_1, \\ \mu_0 &= M_{10}, \quad \mu_1 = M_{11}, \end{aligned} \quad (14)$$

and

$$\begin{aligned} \sigma &= \sigma_0 + \epsilon \tilde{h}_1 \exp(\Sigma t + ikx) \sigma_1, \\ \sigma_0 &= \sqrt{M_{20} - M_{10}^2}, \quad \sigma_1 = \frac{M_{21} - 2M_{10}M_{11}}{2\sqrt{M_{20} - M_{10}^2}}. \end{aligned} \quad (15)$$

Then we set

$$\begin{aligned} D_0(g_0 + \epsilon g_1) + \epsilon h_1 D_1(g_0 + \epsilon g_1) &= \\ D_0(\mu_0 + \epsilon \mu_1 - 2(\sigma_0 + \epsilon \sigma_1)) + \epsilon h_1 D_1(\mu_0 + \epsilon \mu_1 - 2(\sigma_0 + \epsilon \sigma_1)). \end{aligned} \quad (16)$$

Upon linearization in ϵ , we obtain at $\mathcal{O}(1)$

$$D_0(g_0) = D_0(\mu_0 - 2\sigma_0), \quad (17)$$

and restriction of our domain of consideration to the plane below $z = \mu_0$ ¹ immediately implies $g_0 = \mu_0 - 2\sigma_0$. At $\mathcal{O}(\epsilon)$,

$$\begin{aligned} & \frac{\partial D_0}{\partial z} \Big|_{z=g_0} \tilde{g}_1 + D_1(g_0) \tilde{h}_1 = \\ & \tilde{h}_1 \frac{\partial D_0}{\partial z} \Big|_{z=\mu_0-2\sigma_0} \cdot \left(M_{11} - \frac{M_{21} - 2M_{10}M_{11}}{\sqrt{M_{20} - M_{10}^2}} \right) + \tilde{h}_1 D_1 \left(M_{10} - 2\sqrt{M_{20} - M_{10}^2} \right). \end{aligned} \quad (18)$$

Then

$$\frac{\tilde{g}_1}{\tilde{h}_1} = \frac{\frac{\partial D_0}{\partial z} \Big|_{z=\mu_0-2\sigma_0} \cdot \left(M_{11} - \frac{M_{21} - 2M_{10}M_{11}}{\sqrt{M_{20} - M_{10}^2}} \right) + D_1 \left(M_{10} - 2\sqrt{M_{20} - M_{10}^2} \right) - D_1(g_0)}{\frac{\partial D_0}{\partial z} \Big|_{z=g_0}}. \quad (19)$$

This simplifies to

$$\frac{\tilde{g}_1}{\tilde{h}_1} = M_{11} - \frac{M_{21} - 2M_{10}M_{11}}{\sqrt{M_{20} - M_{10}^2}} \equiv \mu_1 - 2\sigma_1. \quad (20)$$

Hence $\frac{\tilde{g}_1}{\tilde{h}_1}$ is expressible *entirely* in terms of the moments of the deposition field. However, previous work [18, 9, 8, 51, 44, 69, 45, 22, 24, 25] typically uses a mean film thickness $h_0(\theta)$ measured against an amorphous-crystalline interface at $z \approx 0$ and lateral phase shift $x_0(\theta)$ between the sinusoidal boundaries. In particular, the lateral phase shift commonly appears as

$$\frac{\tilde{g}_1}{\tilde{h}_1} = \exp(-ikx_0), \quad (21)$$

as in [44, 69, 22, 24, 25]. We must now extract x_0 from Equation (20). In the setting of complex arithmetic,

$$a + bi = re^{i\psi} \quad (22)$$

where $a, b, r, \psi \in \mathbb{R}$, i is the imaginary unit, and ψ is the polar angle in the complex plane. This leads us to equate $x_0 = -\frac{\psi}{k}$, and the factor r that appears will determine the *relative amplitude* between the free and amorphous-crystalline interfaces. Then, formally,

$$\operatorname{Re} \left(M_{11} - \frac{M_{21} - 2M_{10}M_{11}}{\sqrt{M_{20} - M_{10}^2}} \right) + i \operatorname{Im} \left(M_{11} - \frac{M_{21} - 2M_{10}M_{11}}{\sqrt{M_{20} - M_{10}^2}} \right) = r_0 e^{i\psi} \quad (23)$$

where

$$r_0 = \sqrt{\left[\operatorname{Re} \left(M_{11} - \frac{M_{21} - 2M_{10}M_{11}}{\sqrt{M_{20} - M_{10}^2}} \right) \right]^2 + \left[\operatorname{Im} \left(M_{11} - \frac{M_{21} - 2M_{10}M_{11}}{\sqrt{M_{20} - M_{10}^2}} \right) \right]^2} \quad (24)$$

and

$$x_0 = -\frac{1}{k} \arctan \left[\frac{\operatorname{Im} \left(M_{11} - \frac{M_{21} - 2M_{10}M_{11}}{\sqrt{M_{20} - M_{10}^2}} \right)}{\operatorname{Re} \left(M_{11} - \frac{M_{21} - 2M_{10}M_{11}}{\sqrt{M_{20} - M_{10}^2}} \right)} \right]. \quad (25)$$

¹We note that the symmetry of the Gaussian ellipsoid describing implantation into the bulk permits, in principle, two solutions to Equation 17, and we are only interested in solving for the lower one.

Now the linearized amorphous-crystalline interface g is fully characterized by the moments of the deposition field $M_{10}, M_{11}, M_{20}, M_{21}$, and we write

$$\frac{\tilde{g}_1}{\tilde{h}_1} = r_0 \exp(-ikx_0).$$

The above quantity appears repeatedly throughout linear stability analyses of hydrodynamic-type models of ion-induced pattern formation [51, 44, 68, 22, 24, 25].

Amorphous-crystalline interface in physical parameters. Above, calculations were carried out formally. Here, we record h_0, x_0 and r_0 in terms of the basic ion implantation statistics a, α, β . We compute

$$\begin{aligned} M_{10} &= -ac, \\ M_{20} &= c^2 a^2 + (\alpha^2 c^2 + \beta^2 s^2), \\ M_{11} &= \exp\left(-\frac{k^2}{4}((\alpha^2 + \beta^2) - (\alpha^2 - \beta^2) \cos(2\theta))\right) e^{-iaks}, \\ M_{21} &= -2M_{11}c(a - ik(\alpha^2 - \beta^2)s); \end{aligned} \quad (26)$$

and this leads to

$$M_{11} - \frac{M_{21} - 2M_{10}M_{11}}{\sqrt{M_{20} - M_{10}^2}} = M_{11} \left[1 - \frac{2ik(\alpha^2 - \beta^2)sc}{\sqrt{\alpha^2 c^2 + \beta^2 s^2}} \right]. \quad (27)$$

Simplifying the expressions for M_{10}, M_{20}, M_{11} , and M_{21} finally yields

$$\begin{aligned} h_0(\theta) &= -g_0(\theta) = ac + 2\sqrt{\alpha^2 c^2 + \beta^2 s^2}, \\ x_0(\theta; k) &= \frac{1}{k} \arctan \left[\frac{\sin(ak \sin(\theta)) + \frac{2k(\alpha^2 - \beta^2)sc \cos(ak \sin(\theta))}{\sqrt{\alpha^2 c^2 + \beta^2 s^2}}}{\cos(ak \sin(\theta)) - \frac{2k(\alpha^2 - \beta^2)sc \sin(ak \sin(\theta))}{\sqrt{\alpha^2 c^2 + \beta^2 s^2}}} \right], \\ r_0(\theta; k) &= e^{-\frac{k^2}{4}((\alpha^2 + \beta^2) - (\alpha^2 - \beta^2) \cos(2\theta))} \left[1 + \frac{k^2(\alpha^2 - \beta^2)^2 \sin^2(2\theta)}{\alpha^2 c^2 + \beta^2 s^2} \right]. \end{aligned} \quad (28)$$

In the above, we have written $h_0(\theta) = -g_0(\theta)$, representing a change of reference: in the preceding calculations, the upper interface was taken as $z \approx 0$, and we derived the location of the lower interface, $z = g_0(\theta)$. Reverting to the more widely used convention, we subtract $g_0(\theta)$ from the height z of each of the interfaces and then identify $z = -g_0(\theta)$ with the more-conventional $h_0(\theta)$. In Figure 2, $h_0(\theta), x_0(\theta; k)$ and $r_0(\theta; k)$ are plotted for 1000eV Ar⁺-irradiated Si.

Note on discontinuities in $x_0(\theta; k)$. The function $x_0(\theta; k)$ is intended to return the *positive* phase shift between a sinusoidal free interface of wavenumber k , say, $h(x) = \sin(kx)$ and the corresponding sinusoidal amorphous-crystalline interface, say, $g(x) = \sin(k(x - x_0))$. However, when

$$\cos(ak \sin(\theta)) - \frac{2k(\alpha^2 - \beta^2)sc \sin(ak \sin(\theta))}{\sqrt{\alpha^2 c^2 + \beta^2 s^2}} = 0 \quad (29)$$

for some θ , $x_0(\theta; k)$ experiences a jump continuity, leading to non-physical output. To restore the intended physical meaning, one instead computes

$$x_0(\theta; k) = \frac{1}{k} \left(\arctan \left[\frac{\sin(ak \sin(\theta)) + \frac{2k(\alpha^2 - \beta^2)sc \cos(ak \sin(\theta))}{\sqrt{\alpha^2 c^2 + \beta^2 s^2}}}{\cos(ak \sin(\theta)) - \frac{2k(\alpha^2 - \beta^2)sc \sin(ak \sin(\theta))}{\sqrt{\alpha^2 c^2 + \beta^2 s^2}}} \right] + \pi \sum_{j=1}^n \text{He}(\theta - \theta_j^*) \right) \quad (30)$$

where $\text{He}(x)$ is the Heaviside function and θ_j^* is the j^{th} root θ of (29) between 0° and 90° for fixed parameters a, α, β, k . It appears that for *most* physically-realistic parameter combinations (a, α, β, k) (29) has no such roots. In particular, as $k \rightarrow 0$, (29) has no solutions θ for any (a, α, β) . We address the matter here only for mathematical completeness.

Special limits: $k \rightarrow 0, k \rightarrow \infty$. It is clear that $h_0(\theta)$ is independent of wavenumber k , and is therefore expected to be suitable for any perturbation. It is also identical to the result obtained using the “ellipse-dragging” argument of [25]. For arbitrary wavenumber, $x_0(\theta; k)$, on the other hand, depends on k . Using L’Hôpital’s Rule, we recover the $k \rightarrow 0$ limit,

$$x_0(\theta; 0) = a \sin(\theta) + \frac{2(\alpha^2 - \beta^2) \sin(\theta) \cos(\theta)}{\sqrt{\alpha^2 \cos^2(\theta) + \beta^2 \sin^2(\theta)}} \quad (31)$$

as expected. Again for $k \rightarrow 0$, $r_0(\theta; k) \rightarrow 1$, as expected (since this term does not appear in the analysis of [25]). Finally, when $k \rightarrow \infty$, both $r_0(\theta; k) \rightarrow 0$ and $x_0(\theta; k) \rightarrow 0$. This means that the amorphous-crystalline boundary is flat regardless of the shape of the free interface, and the notion of a phase-shift between the free and crystalline-amorphous interfaces loses meaning. We note, however, that the $k \rightarrow \infty$ case is essentially nonphysical, as the period of the free interface cannot physically be smaller than that of the lateral distance occupied by two bonded substrate atoms.

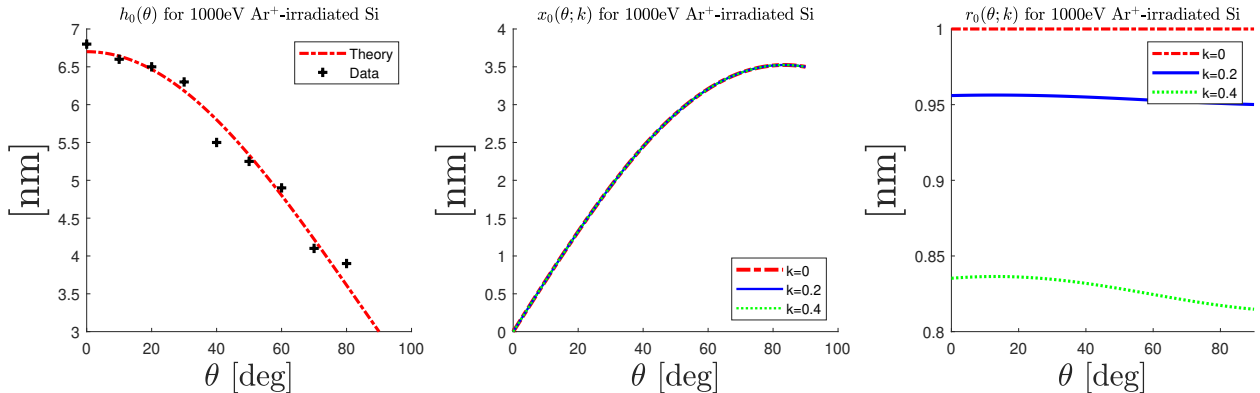


Figure 2: Examples of computed $h_0(\theta)$, $x_0(\theta; k)$ and $r_0(\theta; k)$ based on Equations (28) for 1000keV Ar^+ -irradiated Si. **Left:** comparison of theoretical angle-dependent film thickness with film thickness inferred from experiments [53]. **Center:** the lateral shift separating free and amorphous-crystalline interfaces plotted for three wavenumbers. **Right:** the flattening factor plotted for three wavenumbers.

2.2 Free surface of small curvature

As before, we first consider the flux-diluted deposition integral (1). Now we are interested in developing an approximation of $D(x, z, t)$ valid for small curvature. The small-curvature approximation can then be used to obtain a further simplification in the case of small slopes. Both are expected to be of value for obtaining weakly nonlinear evolution equations for the surface, as in [59, 14, 1, 45].

We first observe that not all ions contribute equally to the value of $D(x, z, t)$ at a fixed but arbitrary point (x, z) . We denote the X -axis domain of influence $[x_L, x_R]$. This domain can be related to the chosen point (x, z) in the bulk as follows: $x - x_L$ must be the distance from x so that

the most distant ellipsoidal implantation region deposits less than 5% of its ions at (x, z) . Observe that $\sigma = 2\sqrt{\alpha^2 s^2 + \beta^2 c^2}$ gives the X -axis extent of the 95th-percentile ellipsoid in line with the collision cascade's center, whose X -axis coordinate is $x_L + as$. As special cases, we note that σ correctly reproduces the limits $\sigma \rightarrow 2\alpha$ when $\theta \rightarrow \frac{\pi}{2}$ and $\sigma \rightarrow 2\beta$ when $\theta \rightarrow 0$. Then the leftmost X coordinate through which an ion could enter and be deposited with a probability of at least 5% at (x, z) is $x_L = x - as - 2\sqrt{\alpha^2 s^2 + \beta^2 c^2}$. A similar argument produces $x_R = x - as + 2\sqrt{\alpha^2 s^2 + \beta^2 c^2}$.

If the slope of $h(X, t)$ changes slowly enough over the interval (x_L, x_R) that the surface admits a linear approximation

$$h(X, t) = h(x, t) + (X - x)h_x \quad (32)$$

over that interval, then a small-curvature approximation of $D(x, z, t)$ is obtained by carrying out the integral

$$\begin{aligned} D(x, z, t) &\approx \frac{\cos(\theta) + h_x \sin(\theta)}{\sqrt{1 + h_x^2}} \int_{-\infty}^{+\infty} \Psi(x, z; X, h(x, t) + (X - x)h_x) dX \\ &= \frac{\Psi_0}{2\pi\alpha\beta} \frac{c + h_x s}{\sqrt{1 + h_x^2}} \int_{-\infty}^{+\infty} e^{\left(-\frac{[(x-X)s-(z-[h(x,t)+(X-x)h_x])c-a]^2}{2\alpha^2} - \frac{[(x-X)c+(z-[h(x,t)+(X-x)h_x])s]^2}{2\beta^2}\right)} dX. \end{aligned} \quad (33)$$

The Gaussian integral above can be computed explicitly using standard techniques to obtain the closed-form approximation

$$D(x, z, t) \approx \frac{\Psi_0}{\sqrt{2\pi}} \frac{c + h_x s}{\sqrt{1 + h_x^2}} \frac{\exp\left[-\frac{(z-h(x,t))+a(c+sh_x))^2}{2\beta^2(s-ch_x)^2+2\alpha^2(c+sh_x)^2}\right]}{\sqrt{\beta^2(s-ch_x)^2 + \alpha^2(c+sh_x)^2}}. \quad (34)$$

Here, we note that all explicit x -dependence has been absorbed into $h(x, t)$. Moreover, if all slopes h_x of interest are small in the laboratory coordinates, then (34) admits a series expansion in $h_x \approx 0$. In the small slope expansion, we recover the “ellipse-dragging” argument of [25]. To leading order in h_x , we again find

$$\begin{aligned} g(x, t) &= h(x - x_0(\theta), t) - (ac + 2\sqrt{\alpha^2 c^2 + \beta^2 s^2}), \\ x_0(\theta) &= a \sin(\theta) + \frac{2(\alpha^2 - \beta^2) \sin(\theta) \cos(\theta)}{\sqrt{\alpha^2 \cos^2(\theta) + \beta^2 \sin^2(\theta)}}, \end{aligned} \quad (35)$$

as in [25]. We also note that linear or quadratic approximations of depth-dependence for ion-induced deformation feature in some of the literature [44, 45, 24]. Following this, we record here the linear approximation of Equation (34) about $z = h(x, t)$,

$$D(x, z, t) \approx D_0(x, z, t) + D_1(x, z, t)(z - h(x, t))$$

where

$$\begin{aligned} D_0(x, z, t) &= \frac{\Psi_0}{\sqrt{2\pi}} \frac{c + h_x s}{\sqrt{1 + h_x^2}} \frac{\exp\left[-\frac{(a(c+sh_x))^2}{2\beta^2(s-ch_x)^2+2\alpha^2(c+sh_x)^2}\right]}{\sqrt{\beta^2(s-ch_x)^2 + \alpha^2(c+sh_x)^2}} \\ D_1(x, z, t) &= \frac{-a(c + h_x s)D_0(x, z, t)}{2s\alpha\beta(c+sh_x)(\alpha^2 - \beta^2) + s^2(h_x^2\alpha^2 + \beta^2) + c^2(h_x^2\beta^2 + \alpha^2)}. \end{aligned} \quad (36)$$

3 Application to continuum model

The above results are mathematically general, describing the distribution of implanted ions through a deformed interface in some special limits. It still remains to connect these results to a continuum model. Here, we briefly consider these analytical results and their implications for an existing continuum model, that of [25]. A more complete treatment will be the subject of forthcoming work. This brief exploration serves two purposes. First, it provides a working example of how the asymptotic results of this work may be applied. Second, it illustrates how hydrodynamic-type models depend rather sensitively on the depth dependence and amorphous-crystalline geometry, which might otherwise be dismissed as minor details of little importance, serving to emphasize the value of the present work.

3.1 Governing equations

The following governing equations describe a particular hydrodynamic model of ion-induced pattern formation. The full details of this model and its development are described elsewhere [51, 69, 22, 24, 25].

Bulk equations. Conservation of mass is applied in the setting of ion-implantation as

$$\nabla \cdot \vec{v} = \frac{\rho}{\rho_a} f A_I \tau_I, \quad (37)$$

where \vec{v} is the Eulerian velocity field, ρ is the density, ρ_a is a basal density of amorphous substrate, f is nominal ion flux, A_I is the per-ion deformation rate due to *ion-induced swelling* (IIS) [69, 22], and $\tau_I = \tau_I(x, z)$ is a dimensionless scalar function of space which modifies the influence of IIS. As an equation of state, we use a “quasi-incompressibility” condition [69],

$$\rho = \frac{\rho_a}{1 + \Delta}, \quad (38)$$

where $\Delta = \Delta(x, z, t)$ is a measure of damage [69, 24], and

$$\frac{\partial \Delta}{\partial t} + \vec{v} \cdot \nabla \Delta = f A_I \tau_I, \quad (39)$$

represents the ongoing accumulation of damage as a parcel of matter advects through the film [69, 22, 24]. Conservation of momentum is written as

$$\nabla \cdot \mathbf{T} = 0, \quad (40)$$

the small-Reynolds number limit of $\rho \left(\frac{\partial \vec{v}}{\partial t} + \vec{v} \cdot \nabla \vec{v} \right) = \nabla \cdot \mathbf{T}$, where \mathbf{T} is the Cauchy stress tensor. Following discussion in [51], we use the Cauchy stress tensor

$$\mathbf{T} = -p \mathbf{I} + 2\eta(\dot{\mathbf{E}} - \tau_D \dot{\mathbf{E}}_b), \quad (41)$$

with $\dot{\mathbf{E}} = \frac{1}{2} (\nabla \vec{v} + \nabla \vec{v}^T)$, the linear strain rate tensor. In the above, p is pressure, η is the viscosity (assumed constant), and \mathbf{I} is the identity tensor. A second effect due to irradiation, *anisotropic plastic flow* (APF) [78, 80, 79, 81, 60, 51], is incorporated through the extra term

$$\dot{\mathbf{E}}_b = f A_D \mathbf{D}(\theta) \equiv f A_D \begin{bmatrix} \frac{3}{2} \cos(2\theta) - \frac{1}{2} & 0 & \frac{3}{2} \sin(2\theta) \\ 0 & 1 & 0 \\ \frac{3}{2} \sin(2\theta) & 0 & -\frac{3}{2} \cos(2\theta) - \frac{1}{2} \end{bmatrix}. \quad (42)$$

Above, A_D is the per-ion deformation due to APF, and $\tau_D = \tau_D(x, z)$ is another dimensionless scalar function which imparts spatial inhomogeneity, analogous to τ_I for IIS. We denote $(\mathbf{D}(\theta))_{ij} = D_{ij}$.

Boundary conditions. At the free upper interface, $z = h(x, t)$, kinematic and stress-balance conditions are applied,

$$v_I = \vec{v} \cdot \hat{\mathbf{n}} - V(\theta) \frac{\rho_c}{\rho} \quad (43)$$

$$[[\mathbf{T}]] \cdot \hat{\mathbf{n}} = \gamma \kappa \hat{\mathbf{n}},$$

where v_I is the interfacial velocity, $\hat{\mathbf{n}}$ is the outward-normal vector from the surface, κ is the mean curvature ($\kappa = \frac{h_{xx}}{(1+h_x^2)^{3/2}}$ in the one-dimensional case), γ is the surface energy (see, e.g., [34]), ρ_c is the crystalline substrate density, and $V(\theta)$ is the downward velocity of the boundary due to erosion [66, 67, 3, 4]. At the lower, amorphous-crystalline interface, $z = g(x, t)$, we apply the no-penetration condition,

$$\vec{v} \cdot \hat{\mathbf{n}} = 0, \quad (44)$$

and the no-slip condition,

$$\vec{v} \cdot \hat{\mathbf{t}} = 0. \quad (45)$$

Here, $\hat{\mathbf{t}}$ is the unit tangent vector from the amorphous-crystalline interface. These are simplifications of the boundary conditions considered in [25], where the effect of phase change at the translating amorphous-crystalline boundary was studied. We neglect these effects in the present work to focus on the amorphous-crystalline interface shape and the effect of depth dependence.

3.2 Linear growth rates

It is frequently of interest to study the short-time (low fluence) evolution of an irradiated surface, when growth (or decay) is exponential [10, 46, 56, 19]. This motivates theoretical analyses of continuum models in the limit of small-amplitude perturbations to the free surface $h(x, t)$ of the form $\epsilon \tilde{h}_1 e^{\Sigma t + i k x}$ where $\epsilon \approx 0$, k is the wavenumber of the perturbation and Σ is a growth rate to be solved for. For general examples, we refer to [21, 12, 16, 15]. For examples relevant to ion-induced nanopatterning, see [58, 3, 65, 4, 18, 51, 50, 8, 9, 44, 69, 45, 56]. Here, we expect that growth rate Σ will depend on irradiation angle θ , flux f , deformation rates A_D and A_I , surface energy γ , viscosity η , implantation parameters a, α, β , and possibly others. For some $\theta_c \in [0^\circ, 90^\circ]$, when $\theta < \theta_c$, $\text{Re}(\Sigma) < 0$, leading to decay of surface perturbations, while for $\theta > \theta_c$, $\text{Re}(\Sigma) > 0$, leading to exponential growth of surface perturbations and the onset of patterning. By computing the fastest-growing wavenumber k as a function of $\theta > \theta_c$, one obtains a theoretical prediction of the wavelengths expected to be observed at short irradiation times. This provides two natural points of comparison with experiments: (i) wavelengths observed at short irradiation times, and (ii) θ_c for the onset of patterning.

Long-wave linear growth rates: depth-dependent IIS. Elsewhere [24], we have obtained general expressions for the low-fluence growth rate Σ for arbitrary depth-dependence of IIS and APF and long-wave perturbations (i.e., $k \approx 0$). Long-wave perturbations are expected to be the most relevant to irradiation-induced patterning [56]. Here, we consider including the depth dependence of IIS, since its mechanism is relatively well-understood, and appears to be related to ion-implantation; see discussion of stress generation in, e.g., [35, 11, 44]. The associated part of the long-wave linear growth rate Σ is

$$\Sigma_I = - \left[\tau_{I,0}(h_0) + h_0 \left\langle \frac{\tau_{I,1}(z)}{\tilde{h}_1} - \frac{1}{2} \iint \frac{\tau_{I,1}(\zeta_2)}{\tilde{h}_1} \frac{d\zeta_2}{h_0} \frac{d\zeta_1}{h_0} \right\rangle - \frac{1}{2} \tau_{I,0}(0) \frac{\tilde{g}_1}{\tilde{h}_1} \right] (kh_0)^2 \quad (46)$$

where $\langle \cdot \rangle$ denotes the average over the domain $z \in [0, h_0]$ and all integrals are also taken over $z \in [0, h_0]$. Hypothesizing that the intensity of IIS depends on the distribution of implanted ions,

or on the defects that result from ion implantation, we now assign to $\tau_{I,0}(z) = D_{f0}(z - h_0)$ and $\tau_{I,1}(z) = \tilde{h}_1 D_{f1}(z - h_0)$, where the transformation $z \rightarrow z - h_0$ is applied to Equation (4), which was originally computed with the macroscopically flat free interface at $z = 0$ rather than $z = h_0$. This ensures compatibility with the conventions used in [24]. Evaluating the above, we obtain the linear dispersion relation associated with IIS

$$\text{Re}(\Sigma_I) \approx -f K_I \frac{\Omega_0(\theta)}{h_0^2(\theta)} (kh_0(\theta))^2 \quad (47)$$

where $K_I = \frac{A_I}{\Psi_0}$, a theoretical conversion factor relating total deposition per ion Ψ_0 to isotropic deformation rate A_I . We take x_0 and h_0 as in Equations (31) and (28), respectively. In the above,

$$\Omega_0(\theta) = \frac{\Psi_0 \cos(\theta)}{\sqrt{8\pi(\alpha^2 c^2 + \beta^2 s^2)}} \left[-2(\alpha^2 c^2 + \beta^2 s^2) \left[\exp\left(\frac{-a^2 c^2}{2(\alpha^2 c^2 + \beta^2 s^2)}\right) - \exp(-2) \right] - ac\sqrt{2\pi(\alpha^2 c^2 + \beta^2 s^2)} \left[\text{erf}\left(\frac{ac}{\sqrt{2(\alpha^2 c^2 + \beta^2 s^2)}}\right) + \text{erf}(\sqrt{2}) \right] \right], \quad (48)$$

where $c = \cos(\theta)$, $s = \sin(\theta)$. The dimensionless coefficient $\frac{\Omega_0(\theta)}{\Psi_0 h_0^2(\theta)}$ characterizes the intensity of IIS due to collision cascade geometry.

Full-spectrum linear growth rates: APF only. Elsewhere [23], a slight extension of the result of [51] was obtained, allowing consideration of how nonplanar boundaries will affect APF in a full-spectrum model where depth-dependence is excluded. For $Q = kh_0$,

$$\begin{aligned} \Sigma_D = & -6f A_D \frac{\cos(2\theta)Q^2}{1 + 2Q^2 + \cosh(2Q)} - 3f A_D \sin(2\theta)(iQ) \\ & - 3f A_D \sin(2\theta)(iQ) \times \frac{\tilde{g}_1}{\tilde{h}_1} \left(\frac{2 \cosh(Q)[Q^2 + \sinh^2(Q)]}{1 + 2Q^2 + \cosh(2Q)} - \cosh(Q) \right) \\ & - \frac{\gamma}{2\eta h_0} \frac{Q(\sinh(2Q) - 2Q)}{1 + 2Q^2 + \cosh(2Q)} \end{aligned} \quad (49)$$

Assigning $\frac{\tilde{g}_1}{\tilde{h}_1}$ and h_0 as in Equations (31) and (28) imparts upon the growth rates the influence of nonplanar boundaries obtained from level sets of the deposition field.

3.3 Weakly nonlinear evolution

Here, we summarize the derivation of a weakly-nonlinear partial differential equation to model the evolving height field. For simplicity, we neglect IIS, focusing on APF only and its depth dependent magnitude will be coupled to the collision cascade, in line with similar considerations made elsewhere [44, 45]. Exploiting the thin-film geometry, we apply the standard lubrication scalings [59, 14, 1]. The scalings and nondimensionalization are applied simultaneously as $x = \frac{h_0 \tilde{x}}{\epsilon}$, $y = \frac{h_0 \tilde{y}}{\epsilon}$, $z = h_0 \tilde{z}$, $t = \frac{h_0 \tilde{t}}{\epsilon u_0}$, $u = u_0 \tilde{u}$, $v = u_0 \tilde{v}$, $w = \epsilon u_0 \tilde{w}$. Here, h_0 is again the angle-dependent film thickness, u_0 is mean lateral flow velocity, and ϵ is a typical, nondimensionalized wave number. For the purposes of later performing an asymptotic expansion, we impose the long-wave limit, $\epsilon \approx 0$. We also nondimensionalize the pressure, surface energy, upper and lower interfaces and ion flux as $p = \frac{\eta u_0 \tilde{p}}{\epsilon h_0}$, $\gamma = \frac{\eta u_0 \tilde{\gamma}}{\epsilon^3}$, $h = h_0 \tilde{h}$, $g = h_0 \tilde{g}$ and $f A = \frac{u_0 \tilde{f} \tilde{A}}{h_0}$. At leading order, and after restricting

attention to the x axis, we have the following. In the interior,

$$\tilde{p}_{0,\tilde{x}} = \tilde{u}_{0,\tilde{z},\tilde{z}} + 2f\tilde{A}_D(D_{11}\tau_{D,\tilde{x}} + D_{13}\tau_{D,\tilde{z}}) \quad (50)$$

$$\tilde{p}_{0,\tilde{z}} = 2f\tilde{A}_DD_{33}\tau_{\tilde{z}} \quad (51)$$

$$\tilde{u}_{0,\tilde{x}} + \tilde{w}_{0,\tilde{z}} = 0. \quad (52)$$

At $\tilde{z} = \tilde{g}$,

$$\tilde{u}_0 = \tilde{w}_0 = 0 \quad (53)$$

and at $\tilde{z} = \tilde{h}$,

$$-\tilde{h}_{\tilde{x}}(-\tilde{p}_0 - 2\tilde{f}A_D\tau_D\tilde{D}_{11}) + \tilde{u}_{0,\tilde{z}} - 2\tilde{f}A_D\tau_D\tilde{D}_{13} = \tilde{\gamma}\tilde{h}_{\tilde{x}}\tilde{h}_{\tilde{x}\tilde{x}} \quad (54)$$

$$-\tilde{p}_0 - 2\tilde{f}A_D\tau_D\tilde{D}_{33} = \tilde{\gamma}\tilde{h}_{\tilde{x}\tilde{x}}. \quad (55)$$

For conciseness and as a simple first study, τ_D is assigned as the further expansion of (36) in small slopes h_x . This results in the assumption of a bulk deposition field linear in both the local free-surface slope h_x and the depth z . Accordingly, we write

$$\tau_D(\tilde{z}, \tilde{h}, \tilde{h}_{\tilde{x}}) = \tau_{D00} + \tau_{D10}\tilde{h}_{\tilde{x}} + \tau_{D01}(\tilde{z} - \tilde{h}) + \tau_{D11}(\tilde{z} - \tilde{h})\tilde{h}_{\tilde{x}}, \quad (56)$$

where $\tau_{D00}, \tau_{D10}, \tau_{D01}$ and τ_{D11} are coefficients involving only s, c, a, α, β :

$$\begin{aligned} \tau_{D00} &= H_1(\alpha^2 c^2 + \beta^2 s^2); \quad \tau_{D01} = H_1 a \cos(\theta) \\ \tau_{D10} &= H_2 \left[1 - \frac{a^2 \beta^2 c^2}{(\alpha^2 c^2 + \beta^2 s^2)^2} \right]; \quad \tau_{D11} = -H_2 \left[\frac{a \beta^2 c ((a^2 - 2\alpha^2)c^2 - 2\beta^2 s^2)}{(\alpha^2 c^2 + \beta^2 s^2)^3} \right] \end{aligned} \quad (57)$$

where

$$H_1 = \frac{2\Psi_0 \cos(\theta) \exp \left[\frac{-a^2}{2(\alpha^2 + \beta^2 \tan^2(\theta))} \right]}{\sqrt{2\pi}(\alpha^2 + \beta^2 + (\alpha^2 - \beta^2) \cos(2\theta))}; \quad H_2 = \frac{\Psi_0 \sin(\theta)}{\sqrt{2\pi}} \exp \left[\frac{-a^2}{2(\alpha^2 + \beta^2 \tan^2(\theta))} \right]. \quad (58)$$

We solve for \tilde{p}_0, \tilde{u}_0 and \tilde{w}_0 by noticing that \tilde{p}_0 can be obtained up to an unknown function of x by integrating $\tilde{p}_{0,\tilde{z}} = 2f\tilde{A}_DD_{33}\tau_{\tilde{z}}$. Then the second boundary condition at $\tilde{z} = \tilde{h}$ is applied to fully determine \tilde{p}_0 . \tilde{u}_0 is found by carrying out two integrations in \tilde{z} of the first momentum balance equation. The two resulting unknown functions of \tilde{x} are determined by using the boundary conditions for \tilde{u}_0 at $\tilde{z} = \tilde{g}$ and $\tilde{z} = \tilde{h}$. We obtain \tilde{w}_0 by integrating conservation of mass and applying the boundary condition at $\tilde{z} = \tilde{g}$. Finally, we substitute into the kinematic condition

$$\tilde{h}_{\tilde{t}} = -\tilde{u}_0\tilde{h}_{\tilde{x}} + \tilde{w}_0, \quad (59)$$

and restore dimensional quantities while assigning $g(x, t) = h(x - x_0(\theta), t) - h_0(\theta) \approx h(x, t) - x_0(\theta)h_x(x, t) - h_0(\theta)$, as in (31). This produces the nonlinear PDE,

$$\begin{aligned} h_t &= C_1 h_{xx} + C_2 h_x h_{xx} + C_3 h_x^2 h_{xx} + C_4 h_x^3 h_{xx} + C_5 h_x^4 h_{xx} + C_6 h_{xx}^2 + C_7 h_x h_{xx}^2 \\ &+ C_8 h_x^2 h_{xx}^2 + C_9 h_x^3 h_{xx}^2 + C_{10} h_{xxx} + C_{11} h_x h_{xxx} + C_{12} h_x^2 h_{xxx} + C_{13} h_x^3 h_{xxx} \\ &+ C_{14} h_x^4 h_{xxx} + C_{15} h_{xx} h_{xxx} + C_{16} h_x h_{xx} h_{xxx} + C_{17} h_x^2 h_{xx} h_{xxx} + C_{18} h_{xxxx} \\ &+ C_{19} h_x h_{xxxx} + C_{20} h_x^2 h_{xxxx} + C_{21} h_x^3 h_{xxxx}, \end{aligned} \quad (60)$$

which describes the temporal evolution of the height field in terms of its own derivatives. For readability, we have suppressed the arguments of, e.g., $C_1 = C_1(\theta, a, \alpha, \beta, f, A, \gamma, \eta)$. We record these coefficients $C_1 - C_{21}$ in the Appendix. The PDE above contains many of the same nonlinearities considered in [61, 26, 64, 45], where interesting parameter-dependent dynamical behavior was observed, including (i) symmetry-breaking [61, 26], (ii) coarsening [61] and saturation of roughness [45], and (iii) angle-dependent reversal of the velocity [45]. At the same time, some nonlinearities in the above do not appear in [45], an alternative model of ion-induced nanopatterning, suggesting nontrivial differences in dynamics.

Ion, target	a [nm]	α [nm]	β [nm]
Ar ⁺ , Si	3.5	1.6	1.5
Kr ⁺ , Si	3.9	1.0	1.2
Xe ⁺ , Si	4.6	0.6	0.9
Ar ⁺ , Ge	2.6	1.6	1.6
Kr ⁺ , Ge	1.7	0.8	0.9
Xe ⁺ , Ge	2.5	0.9	1.0

Table 1: Table of a, α, β , in nm, for the ellipsoidal ion distribution used to obtain the results of the present work. Values estimated using SRIM [86, 85]. Irradiation at 1keV.

4 Results

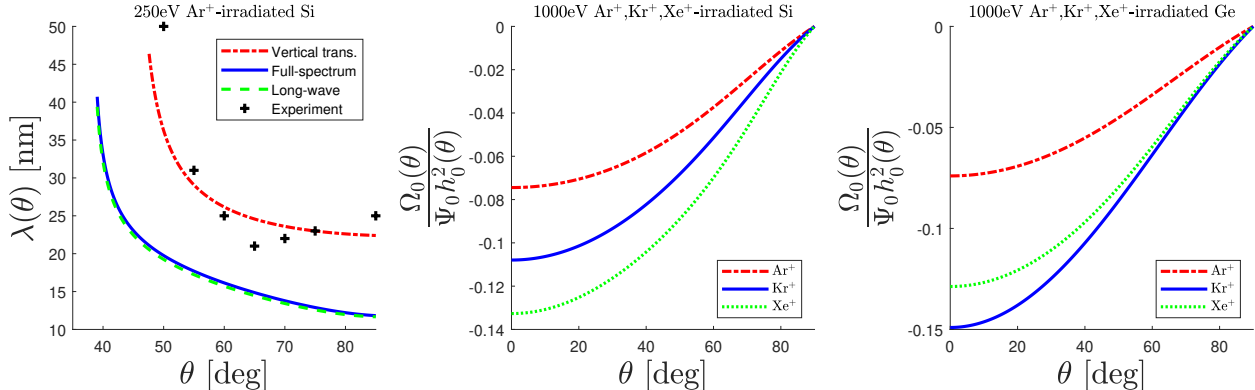


Figure 3: **Left:** Comparison of wavelength $\lambda(\theta)$ predictions from [51] (dash-dotted red curve), experimental data [41], and how they are changed by incorporating the present work. The solid blue curve uses the full-spectrum (arbitrary k) results (28) for the description of the interfaces, while the dashed green curve uses the long-wave ($k \approx 0$) results (31). **Center, right:** Value of the dimensionless coefficient appearing in the linear dispersion relation due to IIS when depth dependence is connected to the distribution of implanted ions for irradiated Si and Ge.

Here we consider the implications of the asymptotic approximations derived above for phenomena in both the linear and nonlinear regimes of pattern formation.

Suppression of ripple growth by IIS. Elsewhere [69, 22, 24], it has been suggested that that ion-induced swelling (IIS) could be an important surface-stabilizing mechanism, leading to

the suppression of pattern formation—or, equivalently, producing higher values of θ_c and larger $\lambda(\theta)$ for fixed $\theta > \theta_c$ than without IIS. Originally taken on a phenomenological basis [69, 22], it appears likely that IIS is simply caused by implanted ions producing isotropic stresses [35, 45]. It is therefore natural to hypothesize that the strength of IIS varies in the amorphous bulk according to the deposition profile of ions. In Figure 3, we consider the implications of this hypothesis by inserting collision cascade parameters a, α, β for each of the systems considered and plotting the dimensionless coefficient $\frac{\Omega_0(\theta)}{\Psi_0 h_0^2(\theta)}$.

We find that, *even for the same total IIS induced per ion, Ψ_0* , some experimental systems are expected to experience stronger surface stabilization due entirely to the depth dependence profile implied by the localized fluence. In particular, the dimensionless coefficient of IIS for Xe^+ -irradiated Si is almost double that of Ar^+ -irradiated Si. The coefficient for Kr^+ -irradiated Si is in-between. Intriguingly, this is consistent with observed trends in θ_c [44].

The per-ion amount of IIS *and* where it occurs in the film both exert a strong influence on the overall pattern suppression effect. For repeated implantation through a patch of the free surface, more compact ellipsoids of implantation, i.e., those with smaller α and β , tend to produce stronger stabilization. The exception is Ar^+ -irradiated Ge, which does not appear to produce patterning [70], while Figure 3 would suggest that IIS-induced stabilization should be *less* strong, hence more permissive of pattern formation. However, (i) other stabilization mechanisms are present, and (ii) it has already been suggested that the ion-target atomic mass ratio must be sufficiently high in order to induce patterning [70].

Wavelength selection. In [51], an analysis of a commonly-used theoretical description of ion-induced surface modification was studied. In Equation (49), we slightly generalize [23] that work to explicitly include the effect of the nonplanar amorphous-crystalline interface in the theorized linear growth rates. In Figure 3, we show the impact of different assumptions about the amorphous-crystalline interface while using, for simplicity, the same parameter values as in [51]: $\gamma = 1.36 \frac{\text{J}}{\text{m}^2}$, $f A_D \eta = 0.25 \text{ GPa}$. In keeping with [51], and to isolate the influence of the amorphous-crystalline boundary shape, we neglect IIS and the possible angle-dependence of the fluidity η^{-1} . We compare wavelength predictions using Equation 49 with $\frac{g_1}{h_1}$ and $h_0(\theta)$ assigned in different ways. First, we use $h_0(\theta) = 3.2 \text{ nm}$, $x_0(\theta) = 0$, $r_0(\theta) = 1$, as in [51]; then we use $x_0(\theta)$ and $h_0(\theta)$ as in Equation 28, where all dependence on k is retained; then we use the long-wave approximation for $x_0(\theta)$ in Equation 31.

Changing from vertically-displaced interfaces, which are nonphysical, to those obtained in Equation 28 leads to reductions in wavelength predictions on the order of 10-20 nm, showing that APF with physically-realistic amorphous-crystalline geometry leads to significantly greater surface destabilization than would otherwise be expected, even while using the same parameter estimates. Hence an additional surface-stabilizing mechanism is needed, such as IIS [69, 22, 24], or angle-dependent fluidity η^{-1} should be considered. This observation would be impossible without a detailed treatment of the interfaces. This raises an important point: exposing the deficiencies of existing models, possibly by showing that they produce worse-than-expected results when more realistic modeling choices are made, is a necessary step in aligning theory and experiment. Finally, we note that there is essentially no difference between the predictions for $\lambda(\theta)$ using the long-wave limit or the full-spectrum expressions for $x_0(\theta; k)$ and $r_0(\theta; k)$; for experimentally observed wavenumbers, the long-wave approximation of the amorphous-crystalline interface appears to be sufficient.

Roughness evolution. The time-evolving root-mean-square (RMS) surface roughness is defined as $R_q(t) = \sqrt{\frac{1}{L} \int_0^L (h(x, t) - \langle h(x, t) \rangle)^2 dx}$ where L is the domain length and $\langle h(x, t) \rangle$ is the mean

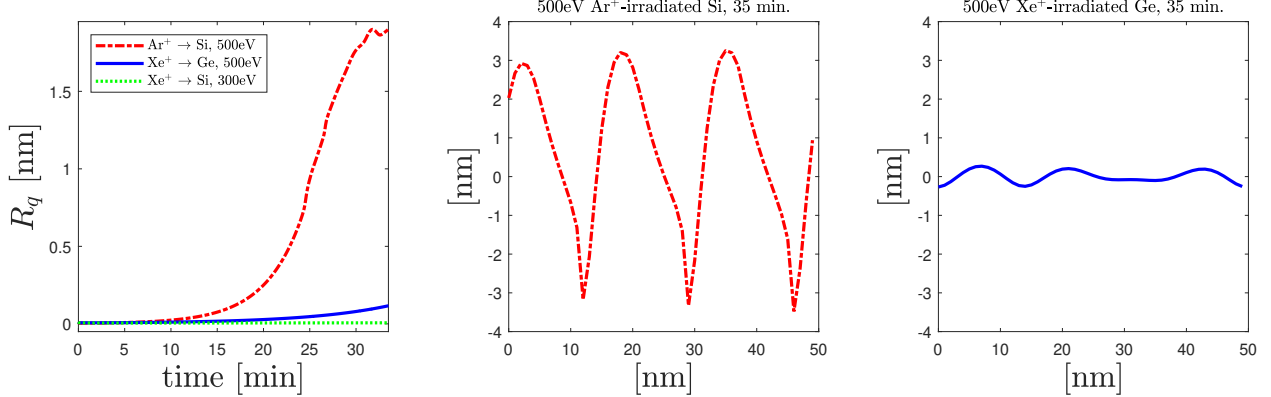


Figure 4: **Left:** simulated time series showing the evolution of surface roughness for three systems where $fA_D = 3 \times 10^{-3} \frac{1}{s}$, $\gamma = 1.36 \frac{J}{m^2}$, $\eta = 100 \text{ GPa} \cdot \text{s}$ and $\theta = 65^\circ$. The only differences are in the assignment of a, α, β . **Center, right:** cross-section of the irradiated surfaces at the same time. For 500eV Ar^+ -irradiated Si, surface roughness has already saturated around 1.9 nm, while the 500eV Xe^+ -irradiated Ge surface is still experiencing exponential growth of ripples.

height at the specified time. This quantity is widely used in the analysis of irradiated surfaces [84, 10, 42, 63, 70, 53, 56, 45] and serves as a valuable point of comparison between theory and experiment. To investigate nonlinear regime phenomena, we numerically integrate (60) with irradiation at $\theta = 65^\circ$, periodic x -axis boundaries and simulated domain of period $L = 50 \text{ nm}$. We use a fourth-order implicit Runge-Kutta scheme and fourth-order central finite differences in space with initial mesh spacing $\Delta x = 1 \text{ nm}$, similar to [46]. The time step is $\Delta t = 10^{-6} \text{ min}$. For initial conditions, we take mean-zero Gaussian white noise with standard deviation 0.01, similar to [61, 26, 45].

As a simple study, we consider surface evolution based on (60) using a, α, β representative of Ar^+ irradiation of Si at 500eV ($a = 2.5, \alpha = 1, \beta = 1.1$), Xe^+ irradiation of Ge at 500eV ($a = 2.0, \alpha = 0.74, \beta = 0.73$), and Xe^+ irradiation of Si at 300eV ($a = 1.76, \alpha = 0.74, \beta = 0.69$) based on SRIM output [85]. Parameters a, α , and β are expressed in nm. Because the focus of the present work is on the importance of the amorphous-crystalline boundary shape and the coevolution of localized ion dose with the free surface, and given the uncertainty surrounding parameter estimation [56], we assign parameter values $fA_D = 3 \times 10^{-3} \frac{1}{s}$, $\gamma = 1.36 \frac{J}{m^2}$, $\eta = 100 \text{ GPa} \cdot \text{s}$ across all simulations, which are comparable to recent estimates [40, 53, 24]. In keeping with the most directly comparable work [45], we do not consider the angle-dependence of the ion-enhanced fluidity, as is sometimes done [53]. We also refrain from exploring the full parametric dependence of (60) on $\theta, a, \alpha, \beta, fA_D, \frac{\gamma}{\eta}$ and the non-linear depth-dependence of the local intensity of APF, which are topics substantial enough to warrant a separate, dedicated study.

Results of these simulations are shown in Figure 4. While it is perhaps unsurprising that non-trivial structures can emerge in light of [26, 61, 45] and related work, some observations can be made. First, while [45] showed sensitivity of surface roughness evolution to parameters explicitly related to ion-induced stress, we show that the amorphous-crystalline interface shape and the localized ion dose exert a significant influence on nonlinear-regime pattern formation *even for a fixed set of parameters fA_D, γ, η* . Second, the shape of the saturated structure for Ar^+ -irradiated Si seen in our Figure 4 is evidently different than those predicted by [45], although the left-right asymmetry of the surface is reproduced.

5 Discussion

Conclusions. In this paper, we have derived asymptotic approximations for the deposition profile of ions in the amorphous bulk and the shape and location of the amorphous-crystalline boundary. These approximations are valid in the limits commonly used for comparison between experimental results and theoretical models: the linear growth regime associated with low fluence, where surface amplitude is small, and the nonlinear growth regime associated with higher fluence, where the surface is typically of small slope in laboratory coordinates. A more complete asymptotic approximation valid for small curvature, but possibly non-small slopes, was also obtained. These results are suitable for use with any of the existing hydrodynamic-type models of irradiation-induced nanopatterning and are intended to facilitate comparison between different theoretical models by reducing the need for *ad hoc* assumptions as to, e.g., the amorphous-crystalline geometry and depth dependence profiles (given the hypothesis that stress production is correlated with the localized dose of radiation, as appears to be the case). Elsewhere [53, 45], the amorphous-crystalline interface shape, its boundary conditions, and the depth-dependence have been suggested as modeling aspects needing refinement, some of which we have provided here.

The incorporation of our asymptotic approximations into models in current use reveals the sensitivity of modeling efforts to seemingly innocuous modeling choices. In particular, we have shown that the plausible hypothesis that ion-induced swelling varies spatially with ion implantation can produce a doubling of the stabilization effect for 1keV Xe^+ -irradiated Si when compared with 1keV Ar^+ -irradiated Si, with Kr^+ -irradiated Si in between. This is broadly consistent with trends observed elsewhere [44], where Xe^+ -irradiated Si has higher θ_c than Ar^+ -irradiated Si.

We then applied the present results to the 250eV Ar^+ -irradiated Si system. When the amorphous-crystalline interface is determined according to our Equation 28, a commonly used phenomenological model of ion-induced surface destabilization [76, 75, 60, 27, 51] selects wavelengths that are much (\sim 10-20nm) smaller when compared with a model assuming vertically-displaced interfaces [51]. While the vertical-displacement assumption appears to lead to better agreement with the data, it is (i) physically incorrect, as can be seen in, for example, [37, 13, 44, 53], and (ii) obscures the fact that the model is missing a stabilizing mechanism that would be needed to produce agreement with experimental observations. This highlights the need for realistic modeling choices in order to avoid illusory agreement between theory and experiment. Usefully, we also find that the long-wave approximation of the amorphous-crystalline geometry is sufficient at most experimentally-observed wavenumbers.

Finally, we have studied a nonlinear partial differential equation for surface evolution where the influence of the amorphous-crystalline geometry and localized, ion-induced stresses are coupled, hypothetically, to the ion implantation profile in the amorphous bulk. This coupling introduces nonlinearities associated with a rich surface dynamics. We also show that roughening rates can be strongly affected by the details of ion implantation and the amorphous-crystalline boundary's geometry; even for the same total implantation, the distribution of implanted ions and resulting lower interface are, on their own, strong contributors to long-term pattern formation. Usefully, the weakly-nonlinear PDE resulting from the present model leads to nonlinearities distinct from those found in related work, e.g., [45]. In particular, our PDE contains nonlinearities of the type shown elsewhere to lead to “mounding” or “kink trains” [26], which are absent in that work. This theoretical prediction may provide a useful point of comparison with experimental work.

Future work and open questions. Studying the coupling between the collision cascade and surface dynamics in viscous flow models will enhance the comparison of theory and experiment by providing greater opportunities for testing hypotheses. Further exploration of this paper's

implications, particularly of the nonlinear PDE (60), will be the subject of forthcoming work. Below, we describe a few areas are of immediate interest.

- We have considered a long-wave model with IIS and a full-spectrum model with APF *separately*. It is clear that, following [24, 25], both mechanisms should be considered together. However, a major obstacle is in determining the deformation rates A_D and A_I , and in understanding how to assign depth-dependence. While it is quite likely that IIS varies with ion implantation, it is unclear what physically causes APF in low-energy systems [51, 62, 53].
- We have obtained a weakly-nonlinear PDE (60) describing surface evolution restricted to the projected downbeam axis and subject to simplifying assumptions described in the main text. Our derivation could easily be extended to obtain the full PDE describing evolution in the plane, which would better facilitate comparison with experimental observations. The full parametric dependence of (60) should be explored and comparisons with experimental observations made, such as [47, 48]. While a great deal of work on the hydrodynamic class of models has focused on the linear growth (low fluence) regime, we suggest that differences in the nonlinearities that emerge from a theoretical model may provide an additional, relatively unexplored, point of comparison with experimental work.
- We have modeled the amorphous-crystalline interface as a level curve of the scalar field representing the localized dose of radiation. While this is physically plausible, leads to good comparison with experimental measurements of the angle-dependent film thickness [25] (see also [44, 13]), and is mathematically convenient, a tacit assumption is that enough damage occurs per collision cascade that the amorphous-crystalline interface never recrystallizes. This assumption would be invalid at very high temperatures or at very low or nonuniform fluxes [10]. In principle, the present analysis could be extended to consider recrystallization and level curves evolving in time. Some work in this direction, although not immediately applicable here, has been done [2, 74, 72, 71, 73].
- The present work has neglected the influence of phase-change at the amorphous-crystalline interface, shown elsewhere to be an important stabilizing mechanism [25]. Incorporation of boundary conditions associated with phase change at the amorphous-crystalline interface leads to additional terms in (60), which have not been considered here. Recrystallization at the boundary could also be modeled. The resulting nonlinear PDEs may display dynamics that are interesting for their own sake.

Acknowledgments

TPE gratefully acknowledges the generous support from the National Science Foundation through DMS-1840260 while at Southern Methodist University and DMS-2136198 while at University of Utah.

A Further calculation details: linear regime

With the linearization described in the main text, the integrand of (1) becomes

$$\begin{aligned} & \frac{\Psi_0 \cos(\theta)}{2\pi\alpha\beta} I_0(x - X, z) + \epsilon \frac{\Psi_0 \cos(\theta)}{2\pi\alpha^3\beta^3} I_0(x - X, z) \left[h_1(X, t) \left(z(\alpha^2 \sin^2(\theta) + \beta^2 \cos^2(\theta)) \right. \right. \\ & \left. \left. + \cos(\theta)\alpha\beta^2 + \cos(\theta)\sin(\theta)(x - X)(\alpha^2 - \beta^2) \right) + \alpha^2\beta^2 \tan(\theta) \frac{\partial h_1(X, t)}{\partial X} \right] + \mathcal{O}(\epsilon^2), \end{aligned} \quad (61)$$

where

$$I_0(x - X, z) = e^{\left(-\frac{[(x-X)\sin(\theta)-z\cos(\theta)-a]^2}{2\alpha^2} - \frac{[(x-X)\cos(\theta)+z\sin(\theta)]^2}{2\beta^2}\right)} \quad (62)$$

We integrate from $X = -\infty$ to $X = +\infty$, facilitated by the change of variables $p := x - X$, so $dX = -dp$. The linearization combined with this change of variables allows us to observe that

$$e^{\Sigma t + ikX} = e^{\Sigma t + ikx} e^{-ikp}; \quad (63)$$

this is useful because we expect the cancellation of a factor of $\exp(ikx + \Sigma t)$ so that we can solve the linearized differential equations in the z coordinate alone, as is typical in such calculations. Now this leads to the linearized deposition field

$$\begin{aligned} D_f(x, z) = & \frac{\Psi_0 \cos(\theta)}{2\pi\alpha\beta} \int_{-\infty}^{\infty} I_0(p, z) dp \\ & + \epsilon \tilde{h}_1 \exp(ikx + \Sigma t) \frac{\Psi_0 \cos(\theta)}{2\pi\alpha^3\beta^3} \left(c_1(z) \int_{-\infty}^{\infty} \exp(-ikp) I_0(p, z) dp + c_2 \int_{-\infty}^{\infty} p \exp(-ikp) I_0(p, z) dp \right) \\ & + \mathcal{O}(\epsilon^2), \end{aligned} \quad (64)$$

where c and s are $\cos(\theta)$ and $\sin(\theta)$ respectively, and

$$\begin{aligned} c_1(z) &= z(\alpha^2 \sin^2(\theta) + \beta^2 \cos^2(\theta)) + \cos(\theta) a \beta^2 + ik\alpha^2 \beta^2 \tan(\theta) \\ c_2 &= \cos(\theta) \sin(\theta) (\alpha^2 - \beta^2). \end{aligned} \quad (65)$$

We compute

$$\begin{aligned} \int_{-\infty}^{\infty} I_0(p, z) dp &= \frac{\sqrt{\pi}}{\sqrt{A}} \exp\left(\frac{B(z)^2}{4A} - C(z)\right); \\ \int_{-\infty}^{\infty} \exp(-ikp) I_0(p, z) dp &= \frac{\sqrt{\pi}}{\sqrt{A}} \exp\left(\frac{\tilde{B}(z)^2}{4A} - C(z)\right); \\ \int_{-\infty}^{\infty} p \exp(-ikp) I_0(p, z) dp &= \frac{-\tilde{B}(z)\sqrt{\pi}}{2A^{3/2}} \exp\left(\frac{\tilde{B}(z)^2}{4A} - C(z)\right), \end{aligned} \quad (66)$$

which leads to the results shown in the main text.

B Further calculation details: weakly-nonlinear PDE

We continue from the main text and summarize the lubrication analysis of Equations (37)-(45).

Bulk equations. With the scalings described in the main text, and many applications of the chain rule, we obtain the dimensionless equations for conservation of mass and momentum,

$$\tilde{u}_{\tilde{x}} + \tilde{v}_{\tilde{y}} + \tilde{w}_{\tilde{z}} = 0 \quad (67)$$

$$\tilde{p}_{\tilde{x}} = 2\epsilon^2 \tilde{u}_{\tilde{x}\tilde{x}} + \epsilon^2 \tilde{u}_{\tilde{y}\tilde{y}} + \tilde{u}_{\tilde{z}\tilde{z}} + \epsilon^2 \tilde{v}_{\tilde{x}\tilde{y}} + \epsilon^2 \tilde{w}_{\tilde{x}\tilde{z}} + 2\tilde{f}\tilde{A}(\tilde{D}_{11}\tau_{D\tilde{x}} + \epsilon\tilde{D}_{12}\tau_{D\tilde{y}} + \tilde{D}_{13}\tau_{D\tilde{z}}) \quad (68)$$

$$\tilde{p}_{\tilde{y}} = \epsilon^2 \tilde{v}_{\tilde{x}\tilde{x}} + 2\epsilon^2 \tilde{v}_{\tilde{y}\tilde{y}} + \tilde{v}_{\tilde{z}\tilde{z}} + \epsilon^2 \tilde{u}_{\tilde{x}\tilde{y}} + \epsilon^2 \tilde{w}_{\tilde{y}\tilde{z}} + 2\tilde{f}\tilde{A}(\epsilon\tilde{D}_{21}\tau_{D\tilde{x}} + \tilde{D}_{22}\tau_{D\tilde{y}} + \tilde{D}_{23}\tau_{D\tilde{z}}) \quad (69)$$

$$\frac{\tilde{p}_{\tilde{z}}}{\epsilon} = \epsilon^3 \tilde{w}_{\tilde{x}\tilde{x}} + \epsilon^3 \tilde{w}_{\tilde{y}\tilde{y}} + 2\epsilon \tilde{w}_{\tilde{z}\tilde{z}} + \epsilon \tilde{u}_{\tilde{x}\tilde{z}} + \epsilon \tilde{v}_{\tilde{y}\tilde{z}} + 2\tilde{f}\tilde{A}(\epsilon\tilde{D}_{31}\tau_{D\tilde{x}} + \epsilon\tilde{D}_{32}\tau_{D\tilde{y}} + \frac{\tilde{D}_{33}}{\epsilon}\tau_{D\tilde{z}}). \quad (70)$$

We note that we have not yet assumed any particular functional form of τ_D , and the factors of ϵ in its coefficients are due to the scaling of the differential operators.

Mass-conservation at amorphous-crystalline interface. From the boundary conditions above, we obtain

$$\begin{aligned}\tilde{u} + \epsilon^2 \tilde{w} \tilde{g}_{\tilde{x}} &= 0 \\ \tilde{v} + \epsilon^2 \tilde{w} \tilde{g}_{\tilde{y}} &= 0 \\ -\tilde{u} \tilde{g}_{\tilde{x}} - \tilde{v} \tilde{g}_{\tilde{y}} + \tilde{w} &= 0\end{aligned}\tag{71}$$

at $\tilde{z} = \tilde{g}$.

Mass-conservation at free interface (kinematic condition). The kinematic condition leads to

$$\tilde{h}_{\tilde{t}} = -\tilde{u} \tilde{h}_{\tilde{x}} - \tilde{v} \tilde{h}_{\tilde{y}} + \tilde{w}.\tag{72}$$

Anticipating that isotropic stresses to compete with the pressure, we scale the diagonal of (42) by $\frac{1}{\epsilon}$, thus introducing $D_{ij} = \tilde{D}_{ij}(1 + (\frac{1}{\epsilon} - 1)\delta_{ij})$ where δ_{ij} is the Kronecker delta. This is consistent with discussion in [59].

Stress balance at free interface. The nondimensionalized stress balance at the upper interface $\tilde{z} = \tilde{h}$ is:

$$\begin{aligned}&\left(-\epsilon \tilde{h}_{\tilde{x}} \left(-\frac{\tilde{p}}{\epsilon} + 2\epsilon \tilde{u}_{\tilde{x}} - 2\frac{\tilde{f} A \tilde{D}_{11} \tau_D}{\epsilon} \right) - \epsilon \tilde{h}_{\tilde{y}} \left(\epsilon \tilde{u}_{\tilde{y}} + \epsilon \tilde{v}_{\tilde{x}} - 2\tilde{f} A \tilde{D}_{12} \tau_D \right) + \tilde{u}_{\tilde{z}} + \epsilon^2 \tilde{w}_{\tilde{x}} - 2\tilde{f} A \tilde{D}_{13} \tau_D \right) \times \\ &\quad \left(1 - (\tilde{h}_{\tilde{x}}^2 + \tilde{h}_{\tilde{y}}^2) \epsilon^2 \right) \\ &= \frac{\tilde{\gamma}}{\epsilon^3} \left(-\epsilon \tilde{h}_{\tilde{x}} \right) \left(\epsilon^2 \tilde{h}_{\tilde{y}\tilde{y}} (1 + \epsilon^2 \tilde{h}_{\tilde{x}}^2) - 2\epsilon^4 \tilde{h}_{\tilde{x}} \tilde{h}_{\tilde{y}} \tilde{h}_{\tilde{x}\tilde{y}} + \epsilon^2 \tilde{h}_{\tilde{x}\tilde{x}} (1 + \epsilon^2 \tilde{h}_{\tilde{y}}^2) \right) \left(1 - 2(\tilde{h}_{\tilde{x}}^2 + \tilde{h}_{\tilde{y}}^2) \epsilon^2 \right),\end{aligned}\tag{73}$$

$$\begin{aligned}&\left(-\epsilon \tilde{h}_{\tilde{y}} \left(-\frac{\tilde{p}}{\epsilon} + 2\epsilon \tilde{v}_{\tilde{y}} - 2\frac{\tilde{f} A \tilde{D}_{22} \tau_D}{\epsilon} \right) - \epsilon \tilde{h}_{\tilde{x}} \left(\epsilon \tilde{v}_{\tilde{x}} + \epsilon \tilde{u}_{\tilde{y}} - 2\tilde{f} A \tilde{D}_{21} \tau_D \right) + \tilde{v}_{\tilde{z}} + \epsilon^2 \tilde{w}_{\tilde{y}} - 2\tilde{f} A \tilde{D}_{23} \tau_D \right) \times \\ &\quad \left(1 - (\tilde{h}_{\tilde{x}}^2 + \tilde{h}_{\tilde{y}}^2) \epsilon^2 \right) \\ &= \frac{\tilde{\gamma}}{\epsilon^3} \left(-\epsilon \tilde{h}_{\tilde{y}} \right) \left(\epsilon^2 \tilde{h}_{\tilde{y}\tilde{y}} (1 + \epsilon^2 \tilde{h}_{\tilde{x}}^2) - 2\epsilon^4 \tilde{h}_{\tilde{x}} \tilde{h}_{\tilde{y}} \tilde{h}_{\tilde{x}\tilde{y}} + \epsilon^2 \tilde{h}_{\tilde{x}\tilde{x}} (1 + \epsilon^2 \tilde{h}_{\tilde{y}}^2) \right) \left(1 - 2(\tilde{h}_{\tilde{x}}^2 + \tilde{h}_{\tilde{y}}^2) \epsilon^2 \right),\end{aligned}\tag{74}$$

$$\begin{aligned}&\left(-\frac{\tilde{p}}{\epsilon} + 2\epsilon \tilde{w}_{\tilde{z}} - 2\frac{\tilde{f} A \tilde{D}_{33} \tau_D}{\epsilon} - \epsilon \tilde{h}_{\tilde{x}} \left(\epsilon^2 \tilde{w}_{\tilde{x}} + \tilde{u}_{\tilde{z}} - 2\tilde{f} A \tilde{D}_{31} \tau_D \right) - \epsilon \tilde{h}_{\tilde{y}} \left(\epsilon^2 \tilde{w}_{\tilde{y}} + \tilde{v}_{\tilde{z}} - 2\tilde{f} A \tilde{D}_{32} \tau_D \right) \right) \times \\ &\quad \left(1 - (\tilde{h}_{\tilde{x}}^2 + \tilde{h}_{\tilde{y}}^2) \epsilon^2 \right) \\ &= \frac{\tilde{\gamma}}{\epsilon^3} \left(\epsilon^2 \tilde{h}_{\tilde{y}\tilde{y}} (1 + \epsilon^2 \tilde{h}_{\tilde{x}}^2) - 2\epsilon^4 \tilde{h}_{\tilde{x}} \tilde{h}_{\tilde{y}} \tilde{h}_{\tilde{x}\tilde{y}} + \epsilon^2 \tilde{h}_{\tilde{x}\tilde{x}} (1 + \epsilon^2 \tilde{h}_{\tilde{y}}^2) \right) \left(1 - 2(\tilde{h}_{\tilde{x}}^2 + \tilde{h}_{\tilde{y}}^2) \epsilon^2 \right).\end{aligned}\tag{75}$$

Leading-order equations. We now expand formally in powers of ϵ ,

$$\begin{aligned}\tilde{u} &= \tilde{u}_0 + \epsilon \tilde{u}_1 + \epsilon^2 \tilde{u}_2 + \mathcal{O}(\epsilon^3) \\ \tilde{v} &= \tilde{v}_0 + \epsilon \tilde{v}_1 + \epsilon^2 \tilde{v}_2 + \mathcal{O}(\epsilon^3) \\ \tilde{w} &= \tilde{w}_0 + \epsilon \tilde{w}_1 + \epsilon^2 \tilde{w}_2 + \mathcal{O}(\epsilon^3) \\ \tilde{p} &= \tilde{p}_0 + \epsilon \tilde{p}_1 + \epsilon^2 \tilde{p}_2 + \mathcal{O}(\epsilon^3)\end{aligned}$$

and we will solve the leading-order equations. At leading order in ϵ , we have the following in the bulk:

$$\tilde{p}_{0,\tilde{x}} = \tilde{u}_{0,\tilde{z},\tilde{z}} + 2f \tilde{A}_D (\tilde{D}_{11} \tau_{0,\tilde{x}} + \tilde{D}_{13} \tau_{0,\tilde{z}}) \quad (76)$$

$$\tilde{p}_{0,\tilde{y}} = \tilde{v}_{0,\tilde{z},\tilde{z}} + 2f \tilde{A}_D (\tilde{D}_{22} \tau_{0,\tilde{y}} + \tilde{D}_{23} \tau_{0,\tilde{z}}) \quad (77)$$

$$\tilde{p}_{0,\tilde{z}} = 2f \tilde{A}_D \tilde{D}_{33} \tau_{0,\tilde{z}} \quad (78)$$

$$\tilde{u}_{0,\tilde{x}} + \tilde{v}_{0,\tilde{y}} + \tilde{w}_{0,\tilde{z}} = 0 \quad (79)$$

At $\tilde{z} = \tilde{g}$, we have

$$\tilde{u}_0 = \tilde{v}_0 = \tilde{w}_0 = 0 \quad (80)$$

and at $\tilde{z} = \tilde{h}$, we have

$$-\tilde{h}_{\tilde{x}}(-\tilde{p}_0 - 2\tilde{f} A_D \tau_D \tilde{D}_{11}) + \tilde{u}_{0,\tilde{z}} - 2\tilde{f} A_D \tau_D \tilde{D}_{13} = \tilde{\gamma} \tilde{h}_{\tilde{x}} (\tilde{h}_{\tilde{x}\tilde{x}} + \tilde{h}_{\tilde{y}\tilde{y}}) \quad (81)$$

$$-\tilde{h}_{\tilde{y}}(-\tilde{p}_0 - 2\tilde{f} A_D \tau_D \tilde{D}_{22}) + \tilde{v}_{0,\tilde{z}} - 2\tilde{f} A_D \tau_D \tilde{D}_{23} = \tilde{\gamma} \tilde{h}_{\tilde{y}} (\tilde{h}_{\tilde{x}\tilde{x}} + \tilde{h}_{\tilde{y}\tilde{y}}) \quad (82)$$

$$-\tilde{p}_0 - 2\tilde{f} A_D \tau_D \tilde{D}_{33} = \tilde{\gamma} (\tilde{h}_{\tilde{x}\tilde{x}} + \tilde{h}_{\tilde{y}\tilde{y}}) \quad (83)$$

While it is possible to collect terms to higher order in ϵ , we will find that surface evolution is already nontrivial even with the leading-order approximation.

Coefficient values. In the main text (60), we have derived the nonlinear PDE

$$\begin{aligned}h_t &= C_1 h_{xx} + C_2 h_x h_{xx} + C_3 h_x^2 h_{xx} + C_4 h_x^3 h_{xx} + C_5 h_x^4 h_{xx} + C_6 h_{xx}^2 + C_7 h_x h_{xx}^2 \\ &\quad + C_8 h_x^2 h_{xx}^2 + C_9 h_x^3 h_{xx}^2 + C_{10} h_{xxx} + C_{11} h_x h_{xxx} + C_{12} h_x^2 h_{xxx} + C_{13} h_x^3 h_{xxx} \\ &\quad + C_{14} h_x^4 h_{xxx} + C_{15} h_{xx} h_{xxx} + C_{16} h_x h_{xx} h_{xxx} + C_{17} h_x^2 h_{xx} h_{xxx} + C_{18} h_{xxxx} \\ &\quad + C_{19} h_x h_{xxxx} + C_{20} h_x^2 h_{xxxx} + C_{21} h_x^3 h_{xxxx}.\end{aligned} \quad (84)$$

The coefficients of the nonlinear PDE are:

$$\begin{aligned}
C_1 &= f A_D h_0^2 \left[\cos(2\theta) \left(3\tau_{00} + 2h_0\tau_{01} \right) - \sin(2\theta) \left(\frac{3}{2}\tau_{10} + h_0\tau_{11} + 3\tau_{00}\frac{x_0}{h_0} + 3\tau_{01}x_0 \right) \right], \\
C_2 &= f A_D h_0^2 \left[\cos(2\theta) \left(6\tau_{10} + 4h_0\tau_{11} + 12\frac{x_0}{h_0}\tau_{00} + 12\tau_{01}x_0 \right) \right. \\
&\quad \left. - \sin(2\theta) \left(6\tau_{10}\frac{x_0}{h_0} + 6\tau_{11}x_0 + 3\tau_{00}\frac{x_0^2}{h_0^2} + 6\tau_{01}\frac{x_0^2}{h_0} \right) \right], \\
C_3 &= f A_D h_0^2 \left[\cos(2\theta) \left(18\tau_{10}\frac{x_0}{h_0} + 18\tau_{11}x_0 + 9\tau_{00}\frac{x_0^2}{h_0^2} + 18\tau_{01}\frac{x_0^2}{h_0} \right) \right. \\
&\quad \left. - \sin(2\theta) \left(\frac{9}{2}\tau_{10}\frac{x_0^2}{h_0^2} + 9\tau_{11}\frac{x_0^2}{h_0} + 3\tau_{01}\frac{x_0^3}{h_0^2} \right) \right], \\
C_4 &= f A_D \left[\cos(2\theta) \left(12\tau_{10}x_0^2 + 24h_0\tau_{11}x_0^2 + 8\tau_{01}x_0^3 \right) - 4\tau_{11}x_0^3 \sin(2\theta) \right], \\
C_5 &= 10f A_D \tau_{11}x_0^3 \cos(2\theta); C_6 = f A_D \left[2h_0^2\tau_{10}x_0 + 3h_0^3\tau_{11}x_0 \cos(2\theta) \right] - \frac{h_0^2\gamma}{\eta}, \\
C_7 &= f A_D \left[4h_0\tau_{10}x_0^2 + 9h_0^2x_0^2\tau_{11} \cos(2\theta) \right] - \frac{4h_0x_0\gamma}{\eta}, \\
C_8 &= f A_D \left[2\tau_{10}x_0^3 + 9\tau_{11}h_0x_0^3 \cos(2\theta) \right] - \frac{3x_0^2\gamma}{\eta}; C_9 = 3f A_D \tau_{11}x_0^4 \cos(2\theta), \\
C_{10} &= f A_D \left[\frac{2}{3}h_0^3\tau_{10} + \frac{3}{4}h_0^4\tau_{11} \cos(2\theta) \right]; C_{11} = f A_D \left[3h_0^3x_0\tau_{11} \cos(2\theta) + 2h_0^2x_0\tau_{10} \right] - \frac{h_0^2\gamma}{\eta}, \\
C_{12} &= f A_D \left[2h_0\tau_{10}x_0^2 + \frac{9}{2}h_0^2\tau_{11}x_0^2 \cos(2\theta) \right] - 2h_0x_0\frac{\gamma}{\eta}, \\
C_{13} &= f A_D \left[\frac{2\tau_{10}x_0^3}{3} + 3h_0x_0^3\tau_{11} \cos(2\theta) \right] - \frac{x_0^2\gamma}{\eta}; C_{14} = \frac{3f A_D x_0^4}{4} \tau_{11} \cos(2\theta), \\
C_{15} &= \frac{-h_0^2x_0\gamma}{\eta}; C_{16} = \frac{-2h_0x_0^2\gamma}{\eta}; C_{17} = \frac{-x_0^3\gamma}{\eta}; C_{18} = \frac{-h_0^3\gamma}{3\eta}, \\
C_{19} &= \frac{-h_0^2x_0\gamma}{\eta}; C_{20} = \frac{-h_0x_0^2\gamma}{\eta}; C_{21} = -\frac{x_0^3\gamma}{3\eta}.
\end{aligned}$$

References

- [1] Vladimir S. Ajaev. *Interfacial Fluid Mechanics: A Mathematical Modeling Approach*. Springer, 2012.
- [2] V.S. Belyakov and A.I. Titov. Stationary amorphous layer formation during 5kev ar+ bombardment of ge. *Radiation Effects and Defects in Solids: Incorporating Plasma Science and Plasma Technology*, 138:231–241, 1996.
- [3] R. M. Bradley and J. M.E. Harper. Theory of ripple topography induced by ion bombardment. *J. Vac. Sci. Technol.*, 6:2390–2395, 1988.
- [4] R. Mark Bradley. Exact linear dispersion relation for the sigmund model of ion sputtering. *Physical Review B*, 84:075413, 2011.

[5] G. Carter. The effects of surface ripples on sputtering erosion rates and secondary ion emission yields. *Journal of Applied Physics*, 85:455–459, 1999. H.

[6] G. Carter, M.J. Nobes, F. Paton, J.S. Williams, and J.L. Whitton. Ion bombardment induced ripple topography on amorphous solids. *Radiation Effects and Defects in Solids: Incorporating Plasma Science and Plasma Technology*, 1977.

[7] G. Carter and V. Vishnyakov. Roughening and ripple instabilities on ion-bombarded Si. *Phys. Rev. B*, 54:17647–17653, 1996.

[8] M. Castro, R. Gago, L. Vázquez, J. Muñoz-García, and R. Cuerno. Stress-induced solid flow drives surface nanopatterning of silicon by ion-beam irradiation. *Physical Review B*, 86:214107, 2012.

[9] Mario Castro and Rodolfo Cuerno. Hydrodynamic approach to surface pattern formation by ion beams. *Applied Surface Science*, 258:4171–4178, 2012.

[10] W. L. Chan and E. Chason. Making waves: Kinetic processes controlling surface evolution during low energy ion sputtering. *J. Appl. Phys.*, 101:121301, 2007.

[11] Wai Lun Chan and Eric Chason. Stress evolution and defect diffusion in Cu during low energy ion irradiation: Experiments and modeling. *J. Vac. Sci. Technol. A*, 26:44, 2008.

[12] Subramanian Chandrasekhar. *Hydrodynamic and Hydromagnetic Instability*. Courier Corporation, 2013.

[13] T. K. Chini, F. Okuyama, M. Tanemura, and K. Nordlund. Structural investigation of keV Ar-ion-induced surface ripples in Si by cross-sectional transmission electron microscopy. *Physical Review B*, 67(205403), 2003.

[14] R. V. Craster and O. K. Matar. Dynamics and stability of thin liquid films. *Rev. Mod. Phys.*, 81:1131–1198, Aug 2009.

[15] M. Cross and H. Greenside. *Pattern Formation and Dynamics in Nonequilibrium Systems*. Cambridge University Press, Cambridge, 2009.

[16] M. C. Cross and P. C. Hohenberg. Pattern formation outside of equilibrium. *Reviews of Modern Physics*, 65:851–1123, 1993.

[17] R. Cuerno and A.-L. Barabási. Dynamic scaling of ion-sputtered surfaces. *Phys. Rev. Lett.*, 74:4746–4749, 1995.

[18] R. Cuerno, M. Castro, J. Muñoz-García, R. Gago, and L. Vásquez. Nanoscale pattern formation at surfaces under ion-beam sputtering: A perspective from continuum models. *Nuclear Instruments and Methods in Physics Research B*, 269:894–900, 2011.

[19] R. Cuerno and J.-S. Kim. A perspective on nanoscale pattern formation at surfaces by ion-beam irradiation. *Journal of Applied Physics*, 128(18):180902, 2020.

[20] C.A. Davis. A simple model for the formation of compressive stress in thin films by ion bombardment. *Thin Solid Films*, 226, 1993.

[21] P.G. Drazin and W.H. Reid. *Introduction to Hydrodynamic Stability*. Cambridge University Press, 1985.

[22] Tyler Evans and Scott Norris. Swelling as a stabilizing mechanism in irradiated thin films ii: Effect of swelling rate. *Journal of Physics: Condensed Matter*, 34:325302, 2022.

[23] Tyler P. Evans. *Viscous thin-film models of nanoscale self-organization under ion bombardment*. PhD thesis, Southern Methodist University, 2023.

[24] Tyler P. Evans and Scott A. Norris. Swelling as a stabilizing mechanism in irradiated thin films: Iii. effect on critical angle in a composite model. *Journal of Physics: Condensed Matter*, 35:325302, 2023.

[25] Tyler P. Evans and Scott A. Norris. Interfacial phase-change and geometry modify nanoscale pattern formation in irradiated thin films. *Journal of Engineering Mathematics*, 146(1):1, Apr 2024.

[26] M. P. Gelfand and R. M. Bradley. One dimensional conservative surface dynamics with broken parity: Arrested collapse versus coarsening. *Physics Letters A*, 379(3):199–205, 2015.

[27] H. B. George, Y. Tang, X. Chen, J. Li, J. W. Hutchinson, J. A. Golovchenko, and M. J. Aziz. Nanopore fabrication in amorphous Si: Viscous flow model and comparison to experiment. *Journal of Applied Physics*, 108:014310, 2010.

[28] Matt P. Harrison and R. Mark Bradley. Crater function approach to ion-induced nanoscale pattern formation: Craters for flat surfaces are insufficient. *Physical Review B*, 89:245401, 2014.

[29] H. Hofsäss, O. Bobes, and K. Zhang. Argon ion beam induced surface pattern formation on Si. *Journal of Applied Physics*, 119:035302, 2016.

[30] Miranda Holmes-Cerfon, Michael J. Aziz, and Michael P. Brenner. Creating sharp features by colliding shocks on uniformly irradiated surfaces. *Physical Review B*, 85:165441, 2012.

[31] Miranda Holmes-Cerfon, Wei Zhou, Andrea L. Bertozzi, Michael P. Brenner, and Michael J. Aziz. Development of knife-edge ridges on ion bombarded surfaces. *Applied Physics letters*, 101:143109, 2012.

[32] M. Z. Hossain, J. B. Freund, and H. T. Johnson. Ion impact energy distribution and sputtering of Si and Ge. *Journal of Applied Physics*, 2012.

[33] Y. Ishii, C. Madi, M. J. Aziz, and E. Chason. Stress evolution in Si during low-energy ion bombardment. *Journal of Materials Research*, 29:2942–2948, 2014.

[34] R. J. Jaccodine. Surface energy of germanium and silicon. *Journal of The Electrochemical Society*, 110(6):524, jun 1963.

[35] N. Kalyanasundaram, M. C. Moore, J. B. Freund, and H. T. Johnson. Stress evolution due to medium-energy ion bombardment of silicon. *Acta Materialia*, 54:483–491, 2006.

[36] G. H. Kinchin and R. S. Pease. The displacement of atoms in solids by radiation. *Reports on Progress in Physics*, 18(1):1, jan 1955.

[37] Tanuj Kumar, Ashish Kumar, Dinesh Chander Agarwal, Nirnajan Prasad Lalla, and Dinnakar Kanjilal. Ion beam-generated surface ripples: new insight in the underlying mechanism. *Nanoscale Research Letters*, 8, 2013.

[38] B. Liedke. *Ion beam processing of surfaces and interfaces: Modeling and atomistic simulations*. PhD thesis, Helmholtz Zentrum Dresden Rossendorf, 2011.

[39] A. Lopez-Cazalilla, D. Chowdhury, A. Ilinov, S. Mondal, P. Barman, S.R. Bhattacharyya, D. Ghose, F. Djurabekova, K. Nordlund, and S. Norris. Pattern formation on ion-irradiated si surface at energies where sputtering is negligible. *Journal of Applied Physics*, 2018.

[40] C. S. Madi. *Linear Stability and Instability Patterns in Ion Bombarded Silicon Surfaces*. PhD thesis, Harvard University, 2011.

[41] C. S. Madi, B. P. Davidovitch, H. B. George, S. A. Norris, M. P. Brenner, and M. J. Aziz. Multiple bifurcation types and the linear dynamics of ion sputtered surfaces. *Phys. Rev. Lett.*, 101:246102, 2008.

[42] C. S. Madi, H. B. George, and M. J. Aziz. Linear stability and instability patterns in ion-sputtered silicon. *J. Phys. Cond. Matt.*, 21:224010, 2009.

[43] Charbel S. Madi and Michael J. Aziz. Multiple scattering causes the low energy-low angle constant wavelength bifurcation of argon ion bombarded silicon surfaces. *Applied Surface Science*, 258:4112–4115, 2012. (IINM2011 Bhubaneswar Conference Proceedings).

[44] A. Moreno-Barrado, M. Castro, R. Gago, L. Vázquez, J. Muñoz-García, R. Redondo-Cubero, B. Galiana, C. Ballesteros, and R. Cuerno. Nonuniversality due to inhomogeneous stress in semiconductor surface nanopatterning by low-energy ion-beam irradiation. *Physical Review B*, 91:155303, 2015.

[45] J. Muñoz-García, R. Cuerno, and Mario Castro. Stress-driven nonlinear dynamics of ion-induced surface nanopatterns. *Phys. Rev. B*, 100:205421, Nov 2019.

[46] J. Muñoz-García, L. Vázquez, M. Castro, R. Gago, A. Redondo-Cubero, A. Moreno-Barrado, and R. Cuerno. Self-organized nanopatterning of silicon surfaces by ion beam sputtering. *Materials Science and Engineering R*, 86:1–44, 2014.

[47] Poco Myint, Karl F. Ludwig, Lutz Wiegart, Yugang Zhang, Andrei Fluerasu, Xiaozhi Zhang, and Randall L. Headrick. Nanoscale dynamics during self-organized ion beam patterning of si. i. ar^+ bombardment. *Phys. Rev. B*, 103:195423, May 2021.

[48] Poco Myint, Karl F. Ludwig, Lutz Wiegart, Yugang Zhang, Andrei Fluerasu, Xiaozhi Zhang, and Randall L. Headrick. Nanoscale dynamics during self-organized ion beam patterning of si. ii. kr^+ bombardment. *Phys. Rev. B*, 103:195424, May 2021.

[49] M. Navez, D. Chaperot, and C. Sella. Microscopie electronique - etude de l'attaque du verre par bombardement ionique. *Comptes Rendus Hebdomadaires Des Seances de l'Academie des Sciences*, 254:240, 1962.

[50] S. A. Norris. Stability analysis of a viscoelastic model for ion-irradiated silicon. *Physical Review B*, 85:155325, 2012.

[51] S. A. Norris. Stress-induced patterns in ion-irradiated silicon: model based on anisotropic plastic flow. *Phys. Rev. B*, 86:235405, 2012.

[52] S. A. Norris, M. P. Brenner, and M. J. Aziz. From crater functions to partial differential equations: A new approach to ion bombardment induced nonequilibrium pattern formation. *J. Phys. Cond. Matt.*, 21:224017, 2009.

[53] S. A. Norris, J. C. Perkinson, M. Mokhtarzadeh, E. Anzenberg, M. J. Aziz, and K. F. Ludwig Jr. Distinguishing physical mechanisms using GISAXS experiments and linear theory: the importance of high wavenumbers. *Scientific Reports*, 7, 2017.

[54] S. A. Norris, J. Samela, L. Bokonte, M. Backman, D. F. K. Nordlund, C.S. Madi, M.P. Brenner, and M.J. Aziz. Molecular dynamics of single-particle impacts predicts phase diagrams for large scale pattern formation. *Nature Communications*, 2:276, 2011.

[55] Scott A. Norris. Pycraters: A python framework for the collection of crater function statistics.

[56] Scott A. Norris and Michael J. Aziz. Ion-induced nanopatterning of silicon: Toward a predictive model. *Applied Physics Reviews*, 6(1):011311, 2019.

[57] Scott A. Norris, J. Samela, K. Nordlund, M. Vestberg, and M. Aziz. Crater functions for compound materials: a route to parameter estimation in coupled-pde models of ion bombardment. *Nuclear Instruments and Methods in Physics Research B*, 318B:245–252, 2014.

[58] S. E. Orchard. On surface levelling in viscous liquids and gels. *Appl. Sci. Res.*, 11A:451, 1962.

[59] Alexander Oron, Stephen H. Davis, and S. George Bankoff. Long-scale evolution of thin liquid films. *Reviews of Modern Physics*, 69:931–980, 1997.

[60] K. Otani, X. Chen, J. W. Hutchinson, J. F. Chervinsky, and M. J. Aziz. Three-dimensional morphology evolution of SiO₂ patterned films under MeV ion irradiation. *J. Appl. Phys.*, 100:023535, 2006.

[61] Daniel A Pearson and R Mark Bradley. Theory of terraced topographies produced by oblique-incidence ion bombardment of solid surfaces. *Journal of Physics: Condensed Matter*, 27(1):015010, dec 2014.

[62] Joy C. Perkinson. *Nanoscale Pattern Self- Organization Under Ion Bombardment*. PhD thesis, Harvard University, 2017.

[63] Joy C. Perkinson, Charbel S. Madi, and Michael J. Aziz. Nanoscale topographic pattern formation on kr+-bombarded germanium surfaces. *Journal of Vacuum Science and Technology A*, 2013.

[64] Joy C. Perkinson, Jennifer M. Swenson, Alexander DeMasi, Christa Wagenbach, Karl F. Ludwig Jr, Scott A. Norris, and Michael J. Aziz. Sawtooth structure formation under nonlinear-regime ion bombardment. *Journal of Physics: Condensed Matter*, 30:no. 30, 2018.

[65] A.S. Rudy and V.K. Smirnov. Hydrodynamic model of wave-ordered structures formed by ion bombardment of solids. *Nuclear Instruments and Methods B*, 159:52–59, 1999.

[66] P. Sigmund. Theory of sputtering. I. Sputtering yield of amorphous and polycrystalline targets. *Phys. Rev.*, 184:383–416, 1969.

[67] P. Sigmund. A mechanism of surface micro-roughening by ion bombardment. *J. Mater. Sci.*, 8:1545–1553, 1973.

[68] Jennifer M. Swenson. *Swelling as a stabilizing mechanism during ion bombardment of thin films: an analytical and numerical study*. PhD thesis, Southern Methodist University, 2018.

[69] Jennifer M Swenson and Scott A Norris. Swelling as a stabilizing mechanism in irradiated thin films. *Journal of Physics: Condensed Matter*, 30(30):304003, July 2018.

[70] Marc Teichmann, Jan Lorbeer, Bashkim Ziberi, Frank Frost, and Bernd Rauschenbach. Pattern formation on ge by low energy ion beam erosion. *New Journal of Physics*, 15:103029, 2013.

[71] A.I. Titov, A.Yu. Azarov, L.M. Nikulina, and S.O. Kucheyev. Mechanism for the molecular effect in si bombarded with clusters of light atoms. *Physical Review B*, 2006.

[72] A.I. Titov, V.S. Belyakov, and A. Yu. Azarov. Formation of surface amorphous layers in semiconductors under low-energy light-ion irradiation: Experiment and theory. *Nuclear Instruments and Methods in Physics Research B*, 212:169–178, 2003.

[73] A.I. Titov, V.S. Belyakov, and A.Yu. Azarov. Damage buildup in semiconductors bombarded by low-energy ions. *Thin Solid Films*, 515:118–121, 2006.

[74] A.I. Titov and S.O. Kucheyev. Ion beam induced amorphous-crystalline phase transition in si: Quantitative approach. *Nuclear Instruments and Methods in Physics Research B*, 168:375–388, 2000.

[75] H. Trinkaus. Dynamics of viscoelastic flow in ion tracks: Origin of plastic deformation of amorphous materials. *Nuclear Instruments and Methods in Physics Research B*, 146:204–216, 1998.

[76] H. Trinkaus and A. I. Ryazanov. Viscoelastic model for the plastic flow of amorphous solids under energetic ion bombardment. *Physical Review Letters*, 75:5072–5075, 1995.

[77] C. C. Umbach, R. L. Headrick, and K.-C. Chang. Spontaneous nanoscale corrugation of ion-eroded SiO₂: The role of ion-irradiation-enhanced viscous flow. *Phys. Rev. Lett.*, 87:246104, 2001.

[78] T. van Dillen, A. Polman, W. Fukarek, and A. van Blaaderen. Energy-dependent anisotropic deformation of colloidal silica particles under mev au irradiation. *Applied Physics Letters*, 78:910–912, 2001.

[79] T. van Dillen, A. Polman, P. R. Onck, and E. van der Giessen. Anisotropic plastic deformation by viscous flow in ion tracks. *Physical Review B*, 71:024103, 2005.

[80] T. van Dillen, A. Polman, C. M. van Kats, and A. van Blaaderen. Ion beam-induced anisotropic plastic deformation at 300 kev. *Applied Physics Letters*, 83:4315–4317, 2003.

[81] T van Dillen, T van der Giessen, P.R. Onck, and A. Polman. Size-dependent ion-beam-induced anisotropic plastic deformation at the nanoscale by nonhydrostatic capillary stresses. *Physical Review B*, 74:132103, 2006.

[82] Werner Wesch and Elke Wendler, editors. *Ion Beam Modification of Solids: Ion-Solid Interaction and Radiation Damage*. Springer, Cham, 2016.

[83] H. Windischmann. An intrinsic stress scaling law for polycrystalline thin films prepared by ion beam sputtering. *Journal of Applied Physics*, 1987.

- [84] B. Ziberi, F. Frost, and B. Rauschenbach. Formation of large-area nanostructures on si and ge surfaces during low energy ion beam erosion. *Journal of Vacuum Science & Technology A*, 24(4):1344–1348, 06 2006.
- [85] J. F. Ziegler and J. P. Biersack. Srim-2000.40, 1984-2000. IBM Co., Yorktown, NY.
- [86] J. F. Ziegler, J. P. Biersack, and U. Littmark. *The Stopping and Range of Ions in Matter*. Pergamon Press, New York, 1985.